Marine Geology 377 (2016) 95–109

Contents lists available at ScienceDirect

Marine Geology

journal homepage: www.elsevier.com/locate/margeo

Reworked tsunami deposits by bottom currents: Circumstantial evidences from Late Pleistocene to Early Holocene in the Gulf of Cádiz

Y. Takashimizu [a,*], R. Kawamura [b], F.J. Rodríguez-Tovar [c], J. Dorador [c], E. Ducassou [d], F.J. Hernández-Molina [e], D.A.V. Stow [f], C.A. Alvarez-Zarikian [g]

[a] Department of Geology, Fac. of Education, Niigata University, Japan
[b] Kamoshida Dai-ichi Elementary School, Yokohama, Japan
[c] Departamento de Estratigrafía y Paleontología, Univ. Granada, 18002 Granada, Spain
[d] Université de Bordeaux, UMR CNRS 5805 EPOC, Allée Geoffroy St Hilaire, 33615 Pessac cedex, France
[e] Department of Earth Sciences, Royal Holloway University London, Egham, Surrey TW20 0EX, UK
[f] IPE, Heriot-Watt University, Edinburgh, Scotland, UK
[g] International Ocean Discovery Program (IODP) and Dept. of Oceanography-Texas A&M University, USA

ARTICLE INFO

Article history:
Received 13 March 2015
Received in revised form 13 September 2015
Accepted 17 September 2015
Available online 23 October 2015

Keywords:
Bi-gradational grading
Bottom current
Contourite
Grain size
Radiocarbon age
Ichnology
Mediterranean outflow water
Tsunami deposits

ABSTRACT

Younger Sand layers (YSLs) have been identified in drill cores of a Late Glacial to Early Holocene muddy contourite succession from the Gulf of Cádiz. In this study, we evaluate the grain size characteristics of the YSL, which display bi-gradational grading, with inverse grading (from silt to fine- or medium-grained sand) followed by normal grading (from fine- or medium-grained sand to silt). Radiocarbon dating shows that the YSL formed at three distinct times: 1) the Bølling-Allerød (sites U1387 and U1386); 2) the Younger Dryas (site U1390), and; 3) the beginning of the Boreal (site U1389). Ichnological analyses and radiocarbon dating of cores from drill site U1389C indicate that the YSLs consist of reworked materials deposited at a high sedimentation rate. The results of sedimentological analyses, ichnological treatment, spatial distributions, and radiocarbon dating of the YSLs suggest that the possibility of an origin of the YSLs is tsunami-related but later reworked by bottom current. However, the source areas of the sandy sediments remain unclear, although our results show them to be variable and area dependent. Some sandy deposits are transported by the Mediterranean Outflow Water (MOW) from the proximal sector of the Gulf of Cádiz Contourite Depositional System (CDS), which is close to the Strait of Gibraltar. However, in other cases it is more probable that local gravity flows, which are the result of instability on adjacent margins, provide the sandy material.

1. Introduction

Contourites are sediments deposited by or significantly affected by bottom current action (e.g., Stow et al., 2002, 2008; Rebesco et al., 2008, 2014). Various contourite facies models have been proposed based on both modern and ancient deposits (e.g., Stow and Lovell, 1979; Faugères et al., 1984; Gonthier et al., 1984; Faugères et al., 1984; Stow and Piper, 1984; Hüneke and Stow, 2008; Stow and Faugères, 2008; Shanmugam, 2012). Recently, Stow and Faugères (2008) proposed an integrated model that recognizes 11 different facies on the basis of their grain size and composition: 1) muddy contourites, 2) silty contourites, 3) sandy contourites, 4) gravel-rich and gravel-bearing contourites, 5) shale-clast or shale-chip layers, 6) volcaniclastic contourites, 7) calcareous muddy and silty contourites, 8) calcareous sandy contourites, 9) calcareous gravel-lag contourites, 10) siliceous bioclastic contourites, and 11) chemogenic contourites. In addition, Stow and Faugères (2008) re-interpreted the Gonthier et al. (1984) original model for contourites, describing five generic contourite sequences based on bioturbated divisions (C1–C5), which include a mud–silt sand sequence characterized by bi-gradational grading. In general, the formation of bi-gradational sequences is thought to be controlled by long-period variations in the mean velocity of the bottom current and by the rate of sediment supply. Rebesco et al. (2014) comprehensively reviewed the study history of contourite facies model from Shanmugam et al. (1993); Martín-Chivelet et al. (2008); Shanmugam (2006a, 2008, 2012), and Stow and Faugères (2008), and introduced examples of the principal sedimentary facies for the contourites recovered during IODP Expedition 339 (Hernández-Molina et al., 2013). Using high-resolution biostratigraphy, oxygen isotope ratios, and radiocarbon data, Stow and Faugères (2008) highlight 2–5 ky cycles of deposition. In contrast, Hüneke and Stow (2008) discuss 2–20 ky cycles, which are possibly Milankovitch in origin. With regard to late Pleistocene Gulf of Cádiz Contourite Depositional System (CDS), Llave et al. (2006) use seismic stratigraphy, long cores, and radiocarbon data to suggest that the formation was linked to Heinrich events

* Corresponding author.

http://dx.doi.org/10.1016/j.margeo.2015.09.009
0025-3227/

and the Younger Dryas. Although similar observations are made by Voelker et al. (2006); Toucanne et al. (2007), and Bahr et al. (2014), the detailed origin of facies-scale sedimentation through time in this region, and the role of bottom currents remains debated.

Between November 2011 and January 2012, the Integrated Ocean Drilling Program (IODP) Expedition 339 drilled five sites in the Gulf of Cádiz, along with two additional sites off the western Iberian margin. They recovered 5.5 km of sediment cores with an average recovery of 86.4%. The Gulf of Cádiz was targeted because it represents a key location for investigating the Mediterranean Outflow Water (MOW), which travels through the Gibraltar Strait and impacts on global circulation and climate (Expedition 339 Scientists, 2012; Hernández-Molina et al., 2013, 2014a, 2014b; Stow et al., 2013b).

In this study, we use grain size analysis, ichnological treatment and accelerator mass spectrometry (AMS) carbon-14 (^{14}C) radiocarbon dating to evaluate younger sand layers (YSLs) found within the Gulf of Cádiz CDS. These units are located below the present-day seafloor sand (PSS), and are intercalated in the Holocene sedimentary successions.

Understanding an origin and features of bi-gradational graded sequence contributes to development of contourite science in the future. YSLs are one of well preserved contourite layer with bi-gradational sequence. For this reason, the main targets of this study are YSLs through Gulf of Cadiz collected by IODP expedition 339. We present a detailed sedimentary stratigraphy that includes a description of bottom current-related sandy deposits. The results of this study will facilitate the more accurate identification of similar deposits in ancient contourites.

2. Regional setting

The southwestern Iberian margin is located near the Azores–Gibraltar Fracture Zone, which is a section of the convergent plate boundary between Eurasia (the Iberian sub-plate) and Africa (the Nubian sub-plate). Plate convergence currently occurs at a rate of ~4–5 mm/y in a WNW-ESE direction. Counter-clockwise rotation along the margin is accommodated by a series of thrust and dextral strike-slip faults (Zitellini et al., 2009; Duarte et al., 2011), active since at least 1.8 Ma. The area is characterized by low–moderate magnitude seismicity (Udías et al., 1976; Grimson and Chen, 1986; Buforn et al., 1995, 2004; Stich et al., 2003, 2005). A number of earthquake-induced tsunami events of historical or pre-historical age are recorded in the sediments of offshore Portugal or in the coastal lowlands of the Gulf of Cádiz (e.g., Gràcia et al., 2010; Lario et al., 2011; Rodríguez-Vidal et al., 2011).

IODP Expedition 339 revealed that the sedimentary evolution of the Gulf of Cádiz, located off the western coast of Portugal, records a detailed history of MOW evolution, extending back to the opening of the Strait of Gibraltar at 5.33 Ma (Hernández-Molina et al., 2014a, 2014b). At present, the MOW results from the mixing of Mediterranean Levantine Intermediate Water and Western Mediterranean Deep Water within the Strait. Upon exiting the Strait, the MOW cascades downslope as a warm saline water overflow (0.67 ± 0.28 Sv; Rogerson et al., 2012) before flowing northwestwards and settling as an intermediate bottom current along the middle slope. Along the middle slope, at water depths of 400–1400 m, two differentiated cores are observed: the Upper Core (MU) and the Lower Core (ML).

The interaction between the MOW and the middle slope of the Gulf of Cádiz generated an extensive CDS, which is divided into five morphosedimentary sectors (Hernández-Molina et al., 2003, 2006; Llave et al., 2006): 1) the proximal scour and ribbons sector, 2) the overflow sedimentary lobe sector, 3) the channels and ridge sector, 4) the contourite depositional sector, and 5) the submarine canyons sector. The development of each of these five sectors relates to the systematic deceleration of the MOW, caused by its interaction with margin bathymetry, as well as the effects of the Coriolis force. In general, the drifts consist mainly of muddy, silty, and sandy sediments with a mixed terrigenous (dominant component) and biogenic composition (Gonthier et al., 1984; Stow et al., 1986, 2002). In contrast, sand and gravel are found in the large contourite channels (Nelson et al., 1993, Nelson et al., 1999; Stow et al., 2013a), along with numerous erosional features (Hernández-Molina et al., 2006; García et al., 2009).

In this study, we use samples from sites U1388, U1389, U1390, U1387, and U1386 (Fig. 1) to document the detailed sedimentological characteristics of the late Pleistocene to Holocene Gulf of Cádiz CDS. Sites U1388, U1387, and U1386 are located under the MU, and sites U1389 and U1390 are distributed within the pathways of the ML. Site U1388 is located ~50 km southwest of the Spanish city of Cádiz in waters with a depth of 663 m. The site lies within the extensive Cádiz sandy sheeted drift and is the closest site to the Strait of Gibraltar. Sites U1389 and U1390 are located within the middle sector of the CDS. Site U1389 is located ~90 km west of Cádiz in waters with a depth of 644 m. It sits on a relative topographic high, which is currently elevated 50–250 m above the flanking contourite channels, ~4 km northwest of the Guadalquivir diapiric ridge. Site U1390 is located ~130 km west of Cádiz in waters with a depth of 992 m. It sits near to the western end of a sheeted drift, which is adjacent to the Guadalquivir Bank and the Guadalquivir contourite channel. It is located 300 m above the channel floor and a little less than 20 km northwest of the of the Guadalquivir diapiric ridge. Site U1387 is located on an elongated mound and is separated from the Faro-Albufeira Drift (hereafter referred to as Faro Drift). It is positioned ~29 km south-southeast of the Portuguese city of Faro in waters with a depth of 559 m. Site U1386 is located at the eastern end of the Faro Drift, less than 25 km south-southeast of Faro, in waters with a depth of 561 m. This site, which lies just 4 km northwest of Site U1387, is the most distal from the Strait of Gibraltar, and represents the most depositional sector within the Gulf of Cádiz CDS.

3. Methodology

3.1. Core descriptions

Sedimentary logs for each drill hole were compiled using a visual core description and high resolution photographs made by scientists on board the Joint Oceanographic Institutions for Deep Earth Sampling (JOIDES) Resolution vessel (Expedition 339 Scientists, 2012; Stow et al., 2013b). Core descriptions are based on sediment textures, composition, type of bed contact, grain size, facies changes, fossil assemblages, and degree of bioturbation.

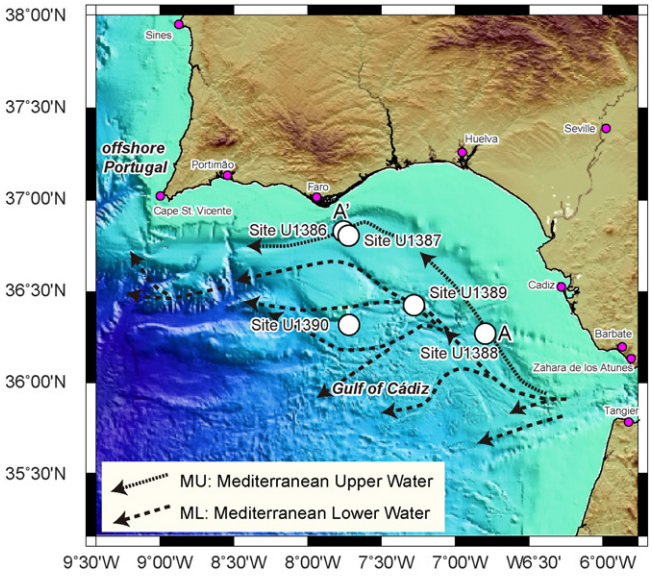

Fig. 1. Index map of the study area. White circles denote drilling sites.

Stratigraphic correlation and age constraints were established onboard using: I) lithostratigraphy, II) biostratigraphy, III) paleomagnetic data, IV) sediment core description, V) geochemical analysis and VI) downhole measurements (Stow et al., 2013b; Hernández-Molina et al., 2014b).

3.2. Sampling

Grain size analyses were completed on 266 samples from 10 drill holes across 5 sites (Tables 1 and 2): at site U1388, 14 samples were analyzed from drill hole A; at site U1389, 30, 23, 24, and 36 samples were analyzed from drill holes A, B, C, and D, respectively; at site U1390, 21 samples were analyzed from drill hole C; at site U1387, 21 and 31 samples were analyzed from drill holes A and B, respectively; at site U1386, 20 and 46 samples were analyzed from drill holes A and B, respectively. Samples were extracted from the cores at 50 cm intervals downward from the seafloor. However, with the exception of site U1386B, samples within the YSL (positioned between the upper and lower muddy layers) were taken at ~2.5 cm intervals. At site U1386B, samples were extracted at ~1 cm intervals in order to obtain more detailed vertical profile of variations in grain size.

3.3. Grain size

Grain size analyses were conducted using a Mastersizer 3000 laser diffraction particle size analyzer (Malvern Instruments Ltd.) equipped with a Hydro LV unit at Niigata University. The measurement range for grain size analysis was 0.01–2100 μm. Particles were separated using an ultrasonic dispersion treatment in which samples were placed in a water solution containing 0.2 wt.% sodium hexametaphosphate for 3 min. The refractive index was set to 1.572 and the absorption index was set to 1.330. Measurement time was 5 s per sample for both the red and blue lasers and measurements were repeated 5 times. The optimal obscuration for the measurements ranged between 8 and 20%.

Five grain size parameters (D_{10}: 10th percentile grain size; GM: geometric mean grain size; Md: median grain size; Mo: mode grain size; D_{90}: 90th percentile grain size) and one sorting parameter (GSD: geometric standard deviation) were calculated using the Malvern Mastersizer software (version 3.1). GM and GSD are calculated using the moment method, as follows:

$$GM = \exp\left\{\frac{\sum(\ln P_i \cdot d_i)}{100}\right\} \quad (1)$$

$$GSD = \exp\left\{\sqrt{\sum(\ln(p_i))^2 \cdot d_i - (\ln(GM))^2}\right\} \quad (2)$$

where p_i is the proportion of the result in bin i. Average particle size is in μm.

3.4. AMS radiocarbon dating

Eleven planktonic foraminifera samples were dated using the AMS facility of the Geo Science Laboratory Co. Ltd. (Nagoya, Japan) and Laboratoire de Mesure du Carbone 14 (Saclay, Paris, France). Six samples were sourced from site U1389C, two samples from site U1390B, one sample from U1390C, one sample from site U1387A, and one sample from site U1386A. Radiocarbon ages were converted to calibrated years before present (cal. y BP) using calibration data (Talma and Vogel, 1993). MARINE13 calibration curves (Reimer et al., 2013) were used for planktonic foraminifera samples using the CALIB radiocarbon calibration software (version 7.0.1; Stuiver and Reimer, 1993).

3.5. Ichnological treatment

General information about the degree of bioturbation (sparse, slight) has been included in the lithological description of all the studied holes. For drill holes A–D of site U1389, trace fossil analyses were conducted for both the YSL and for the under and overlying mud layers. Analyses were carried out at intervals of 5.15–5.65 m below the seafloor (mbsf) at drill hole A; 3.35–4.15 mbsf at drill hole B; 4.65–5.36 mbsf at drill hole C, and; 4.65–5.32 mbsf at drill hole D.

Ichnological analyses were conducted following digital image treatment (Dorador and Rodríguez-Tovar, 2014; Dorador et al., 2014a, 2014b; Rodríguez-Tovar and Dorador, 2014, in press). Several digital

Table 1
Summary of site details.

Site name	U1388	U1389				U1390
Hole name	A	A	B	C	D	B
Latitude	36°16.1378 N	36°25.5183 N	36°25.5199 N	36°25.5199 N	36°25.5092 N	36°19.1460 N
Longitude	006°47.6602 W	007°16.6907 W	007°16.6772 W	007°16.6772 W	007°16.6772 W	007°43.0815 W
Water depth (m)	663.6	644.7	643.9	642.9	644.0	990.7
Number of samples	14	30	23	24	36	0
Depth (mbsf)						
Studied interval	0.000–7.000	0.000–7.000	0.000–5.000	0.000–8.000	0.000–8.000	0.000–8.500
Present seafloor sand (PSS)	0.000–7.000	0.000–1.700	N/A	N/A	N/A	N/A
Younger sand layer (YSL)	N/A	5.225–5.595	3.448–3.998	4.720–5.300	4.700–5.330	6.630–6.750
Second sand layer (SSL)	N/A	N/A	N/A	7.090–7.280	6.640–6.870	N/A

Site name		U1387		U1386	
Hole name	C	A	B	A	B
Latitude	36°19.1466 N	36°48.3246 N	36°48.3246 N	36°49.6885 N	36°49.6880 N
Longitude	007°43,674 W	007°43.1408 W	007°43.1278 W	007°45.3309 W	007°45.3168 W
Water depth (m)	992.4	559.1	558.2	560.4	561.9
Number of samples	21	21	31	20	46
Depth (mbsf)					
Studied interval	0.000–8.000	0.000–5.000	0.000–5.000	0.000–5.000	0.000–5.000
Present seafloor sand (PSS)	N/A	N/A	N/A	N/A	N/A
Younger sand layer (YSL)	6.625–6.800	2.000–2.375	1.970–2.290	2.645–2.920	2.370–2.710
Second sand layer (SSL)	N/A	N/A	N/A	N/A	N/A

Table 2
Samples extracted from cores.

Sample name	Depth (mbsf)	Sample name	Depth (mbsf)	Sample name	Depth (mbsf)	Sample name	Depth (mbsf)
U1388A1H1W0-2	0.000	U1389C1H4W23-25	4.720	U1390C1H3W50-52	3.500	U1386A1H1W50-52	0.500
U1388A1H1W50-52	0.500	U1389C1H4W25-27	4.750	U1390C1H3W100-102	4.000	U1386A1H1W100-102	1.000
U1388A1H1W100-102	1.000	U1389C1H4W27.5–29.5	4.775	U1390C2H2W10-12	6.000	U1386A1H2W0-2	1.500
U1388A1H1W134-136	1.340	U1389C1H4W30-32	4.800	U1390C2H2W60-62	6.500	U1386A1H2W50-52	2.000
U1388A1H1W136-138	1.360	U1389C1H4W32.5–34.5	4.825	U1390C2H2W70.5–72.5	6.605	U1386A1H2W100-102	2.500
U1388A1H1W138.5–140.5	1.385	U1389C1H4W35-37	4.850	U1390C2H2W72.5–74.5	6.625	U1386A1H2W114.5–116.5	2.645
U1388A1H1W141-143	1.410	U1389C1H4W37.5–39.5	4.875	U1390C2H2W75-77	6.650	U1386A1H2W116.5–118.5	2.665
U1388A1H1W143.5–145.5	1.435	U1389C1H4W40-42	4.900	U1390C2H2W77.5–79.5	6.675	U1386A1H2W119-121	2.690
U1388A1H1W146-148	1.460	U1389C1H4W42.5–44.5	4.925	U1390C2H2W80-82	6.700	U1386A1H2W121.5–123.5	2.715
U1388A1H2W0-2	1.500	U1389C1H4W45-47	4.950	U1390C2H2W82.5–84.5	6.725	U1386A1H2W124-126	2.740
U1388A1H2W50-52	2.000	U1389C1H4W47.5–49.5	4.975	U1390C2H2W85-87	6.750	U1386A1H2W126.5–128.5	2.765
U1388A1H2W100-102	2.500	U1389C1H4W50-52	5.000	U1390C2H2W87.5–89.5	6.775	U1386A1H2W129-131	2.790
U1388A1H3W19-21	3.000	U1389C1H4W52.5–54.5	5.025	U1390C2H2W90.0–92.0	6.800	U1386A1H2W131.5–133.5	2.815
U1388A1H4W8-10	3.500	U1389C1H4W55-57	5.050	U1390C2H2W110-112	7.000	U1386A1H2W134-136	2.840
U1389A1H1W0-2	0.000	U1389C1H4W57.5–59.5	5.075	U1387A1H1W0-2	0.000	U1386A1H2W136.5–138.5	2.865
U1389A1H1W50-52	0.500	U1389C1H4W60-62	5.100	U1387A1H1W50-52	0.500	U1386A1H2W139.5–141.5	2.895
U1389A1H1W100-102	1.000	U1389C1H4W62.5–64.5	5.125	U1387A1H1W100-102	1.000	U1386A1H2W142-144	2.920
U1389A1H2W0-2	1.500	U1389C1H4W65-67	5.150	U1387A1H2W0-2	1.500	U1386A1H3W0-2	3.000
U1389A1H2W50-52	2.000	U1389C1H4W67.5–69.5	5.175	U1387A1H2W50-52	2.000	U1386A1H3W50-52	3.500
U1389A1H2W100-102	2.500	U1389C1H4W70-72	5.200	U1387A1H2W53-55	2.030	U1386B1H1W0-2	0.000
U1389A1H3W0-2	3.000	U1389C1H4W72.5–74.5	5.225	U1387A1H2W55-57	2.050	U1386B1H1W50-52	0.500
U1389A1H3W50-52	3.500	U1389C1H4W75-76	5.250	U1387A1H2W57.5–59.5	2.075	U1386B1H1W100-102	1.000
U1389A1H3W100-102	4.000	U1389C1H4W77.5–79.5	5.275	U1387A1H2W60-62	2.100	U1386B1H2W0-2	1.500
U1389A2H1W20-22	4.500	U1389C1H4W80-82	5.300	U1387A1H2W62.5–64.5	2.125	U1386B1H2W50-52	2.000
U1389A2H1W70-72	5.000	1389D1H1W0-2	0.000	U1387A1H2W65-67	2.150	U1386B1H2A93.5–95.5	2.435
U1389A2H1W92.5–94.5	5.225	1389D1H1W50-52	0.500	U1387A1H2W67.5–69.5	2.175	U1386B1H2A95.5–96.5	2.455
U1389A2H1W94.5–96.5	5.245	1389D1H1W100-102	1.000	U1387A1H2W70-2	2.200	U1386B1H2A96.5–97.5	2.465
U1389A2H1W97-98	5.270	1389D1H2W0-2	1.500	U1387A1H2W72.5–74.5	2.225	U1386B1H2A97.5–98.5	2.475
U1389A2H1W99.5–101.5	5.295	1389D1H2W50-52	2.000	U1387A1H2W75-77	2.250	U1386B1H2A98.5–99.5	2.485
U1389A2H1W102-104	5.320	1389D1H2W100-102	2.500	U1387A1H2W77.5–79.5	2.275	U1386B1H2A99.5–100.5	2.495
U1389A2H1W104.5–106.5	5.345	1389D1H3W0-2	3.000	U1387A1H2W80-82	2.300	U1386B1H2A100.5–101.5	2.505
U1389A2H1W107-109	5.370	1389D1H3W50-52	3.500	U1387A1H2W82.5–84.5	2.325	U1386B1H2A101.5–102.5	2.515
U1389A2H1W109.5–111.5	5.395	1389D1H3W100-102	4.000	U1387A1H2W85-87	2.350	U1386B1H2W102-104	2.525
U1389A2H1W112-114	5.420	U1389D1H4W0-2	4.500	U1387A1H2W87.5–89.5	2.375	U1386B1H2A102.5–103.5	2.530
U1389A2H1W114.5–116.5	5.445	U1389D1H4W20.5–22.5	4.700	U1387A1H2W100-102	2.500	U1386B1H2A103.5–104.5	2.535
U1389A2H1W117-119	5.470	U1389D1H4W22.5–24.5	4.725	U1387B1H1W0-2	0.000	U1386B1H2A104.5–105.5	2.545
U1389A2H1W119.5–121.5	5.495	U1389D1H4W25-26	4.750	U1387B1H1W50-52	0.500	U1386B1H2A105.5–106.5	2.555
U1389A2H1W122-124	5.520	U1389D1H4W27.5–29.5	4.775	U1387B1H1W100-102	1.000	U1386B1H2A106.5–107.5	2.565
U1389A2H1W124.5–126.5	5.545	U1389D1H4W30-32	4.800	U1387B1H2W0-2	1.500	U1386B1H2A107.5–108.5	2.575
U1389A2H1W127-129	5.570	U1389D1H4W32.5–34.5	4.825	U1387B1H2W47-49	1.970	U1386B1H2A108.5–109.5	2.585
U1389A2H1W129.5–131.5	5.595	U1389D1H4W35-37	4.850	U1387B1H2A49-51	1.990	U1386B1H2W109.5–110.5	2.595
U1389A2H2W20-22	6.000	U1389D1H4W37.5–39.5	4.875	U1387B1H2A51.5–53.5	2.015	U1386B1H2A110.5–111.5	2.605
U1389A2H2W70-72	6.500	U1389D1H4W40-42	4.900	U1387B1H2A54-56	2.040	U1386B1H2A111.5–112.5	2.615
U1389A2H2W123-125	7.030	U1389D1H4W42.5–44.5	4.925	U1387B1H2A56.5–58.5	2.065	U1386B1H2A112.5–113.5	2.625
U1389B1H3W45.5–47.5	3.455	U1389D1H4W45-46	4.950	U1387B1H2A59-61	2.090	U1386B1H2W113-114	2.630
U1389B1H3W47.5–49.5	3.475	U1389D1H4W47.5–49.5	4.975	U1387B1H2A61.5–63.5	2.115	U1386B1H2A113.5–114.5	2.635
U1389B1H3W50-52	3.500	U1389D1H4W50-52	5.000	U1387B1H2A64-66	2.140	U1386B1H2A114.5–115.5	2.645
U1389B1H3W52.5–54.5	3.525	U1389D1H4W52.5–54.5	5.025	U1387B1H2A66.5–68.5	2.165	U1386B1H2A115.5–116.5	2.655
U1389B1H3W55-57	3.550	U1389D1H4W55-57	5.050	U1387B1H2A69-71	2.190	U1386B1H2A116.5–117.5	2.665
U1389B1H3W57.5–59.5	3.575	U1389D1H4W57.5–59.5	5.075	U1387B1H2A71.5–73.5	2.215	U1386B1H2W117-118	2.670
U1389B1H3W60-62	3.600	U1389D1H4W60-62	5.100	U1387B1H2A74-76	2.240	U1386B1H2A117.5–118.5	2.675
U1389B1H3W62.5–64.5	3.625	U1389D1H4W62.5–64.5	5.125	U1387B1H2A76.5–78.5	2.265	U1386B1H2A118.5–119.5	2.685
U1389B1H3W65-67	3.650	U1389D1H4W65-67	5.150	U1387B1H2W79-81	2.290	U1386B1H2A119.5–120.5	2.695
U1389B1H3W67.5–69.5	3.675	U1389D1H4W67.5–69.5	5.175	U1387B1H2W100-102	2.500	U1386B1H2A120.5–121.5	2.705
U1389B1H3W71-73	3.710	U1389D1H4W70-72	5.200	U1387B1H3W0-2	3.000	U1386B1H2A121.5–122.5	2.715
U1389B1H3W73.5–75.5	3.735	U1389D1H4W72.5–74.5	5.225	U1387B1H3W50-52	3.500	U1386B1H2A122.5–124.5	2.725
U1389B1H3W79-81	3.790	U1389D1H4W75-77	5.250	U1387B1H3W100-1.02	4.000	U1386B1H3W0-2	3.000
U1389B1H3W81.5–83.5	3.815	U1389D1H4W77.5–79.5	5.275	U1387B1H4W0-2	4.500	U1386B1H3W50-52	3.500
U1389B1H3W84-86	3.840	U1389D1H4W80-82	5.300	U1387B1H4W50-52	5.000	U1386B1H3W100-102	4.000
U1389B1H3W86.5–88.5	3.865	U1389D1HCCW15-17	5.330	U1387B1H4W100-102	5.500	U1386B1H4W0-0	4.500
U1389B1H3W89-91	3.890	U1390C1H1W0-2	0.000	U1387B1H5W0-2	6.000	U1386B1H4W50-52	5.000
U1389B1H3W91.5–93.5	3.915	U1390C1H1W50-52	0.500	U1387B1H5W50-52	6.500	U1386B1H4W100-102	5.500
U1389B1H3W94-96	3.940	U1390C1H1W100-102	1.000	U1387B1H5W100102	7.000	U1386B1H5W0-2	6.000
U1389B1H3W96.5–98.5	3.965	U1390C1H2W0-2	1.500	U1387B1H6W0-2	7.500	U1386B1H5W50-52	6.500
U1389B1H3W99-101	3.990	U1390C1H2W50-52	2.000	U1387B1H6W50-52	8.000	U1386B1H5W100-102	7.000
U1389B1H3W101.5–103.5	4.015	U1390C1H2W100-102	2.500	U1387B1H6W100-102	8.500		
U1389B1H3W104-106	4.040	U1390C1H3W0-2	3.000	U1386A1H1W0-2	0.000		

image analysis techniques were applied to improve the visibility of bioturbational sedimentary structures (e.g., biodeformational structures and trace fossils), as well as to evaluate degrees of bioturbation. These methods are based on the modification of high-resolution digital images (e.g., brightness and vibrance), together with the characterization of pixel values.

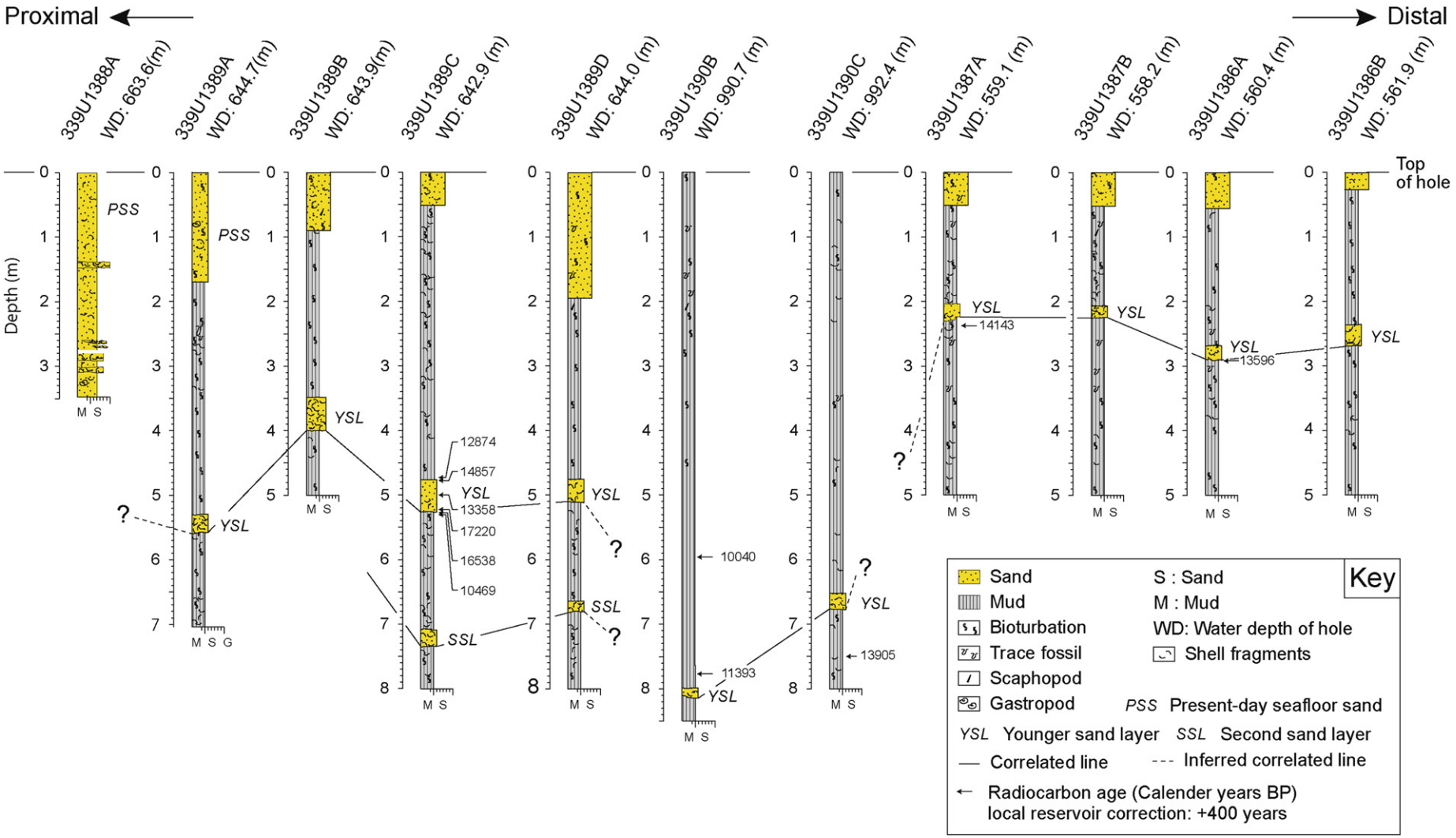

Fig. 2. Stratigraphic columns of the studied cores. Unit ages in years before present (BP) are based on radiocarbon dating.

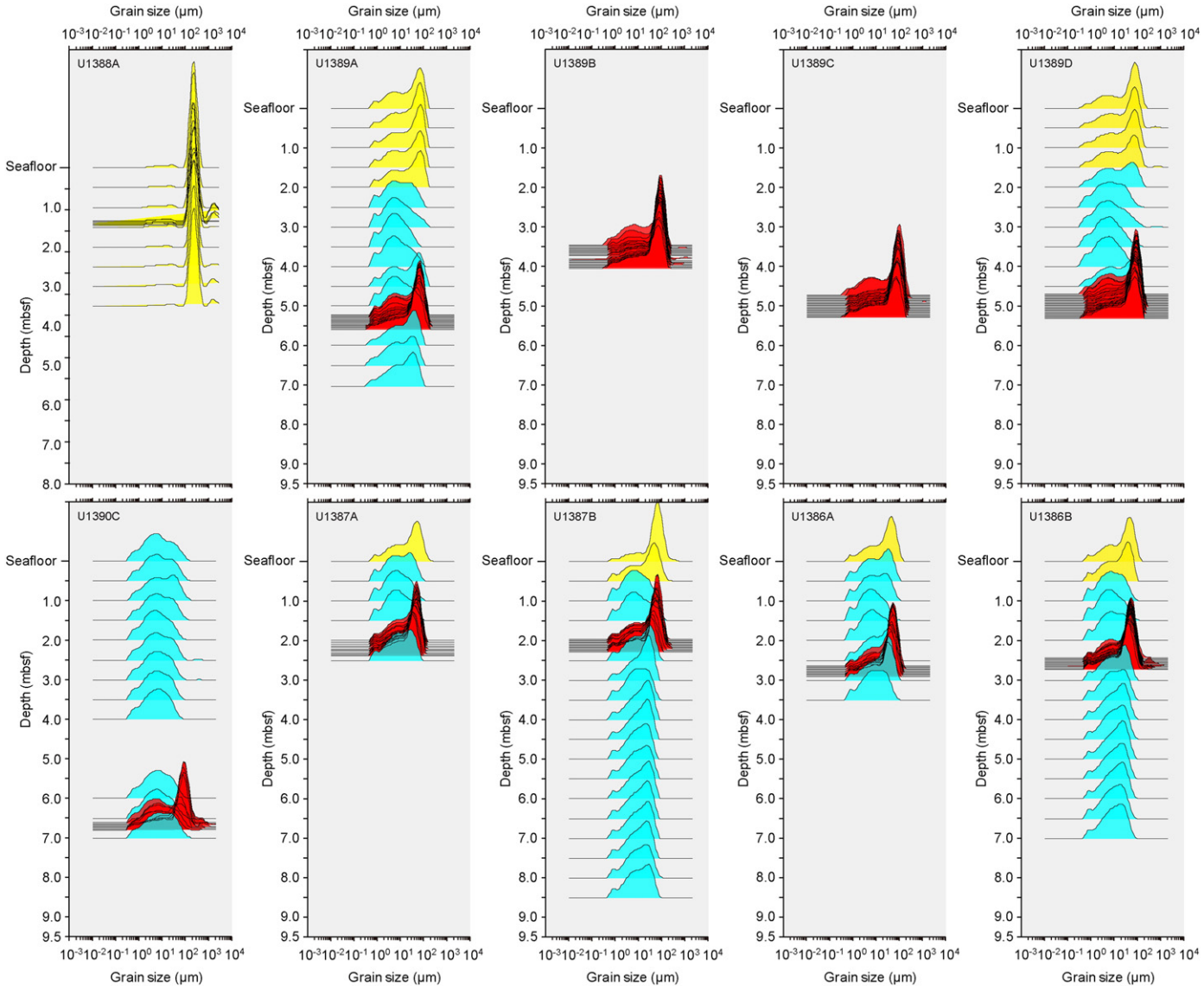

Fig. 3. Vertical variations in grain size distribution for each of the studied cores.

4. Results

4.1. Lithological and grain size features

Most of the sediments in this study consist of mud and silt materials. However, one or two sand layers are intercalated between the mud and silt-rich sediments. The sandy layers are characterized by: 1) well sorted material; 2) low amounts of bioturbation (although this is also common in the overlying and underlying deposits); 3) bi-gradational grading, and; 4) "soupy sand", which has a high water content.

4.1.1. Drill hole U1388A (seafloor–3.5 mbsf)

The sediments of the U1388A core mainly consist of fine sands with biogenic carbonate (Figs. 2 and 3). The top and base contacts are sharp and shell fragments and bioturbation are sparse. The YSL consists of a calcareous medium sand layer with common shell fragments intercalated at 1.360–1.500 mbsf, and calcareous fine sand layers with common shell fragments and rare bioturbation intercalated at 2.61–2.66 mbsf, 2.81–2.94 mbsf, and 3.01–3.11 mbsf. A complete gastropod is preserved between 3.27 and 3.29 mbsf.

With regard to vertical variations in grain size characteristics (Fig. 4), the GM of the calcareous medium sand layer with common shell fragments (1.360–1.500 mbsf) displays inverse grading from fine–medium sand (1.435–1.500 mbsf), and then normal grading from medium–fine sand (1.360–1.435 mbsf). The other grain size characteristics (D_{10}, Md, and Mo) indicate a similar trend in vertical variations. D_{90} shows large vertical variation with inverse grading from fine–very coarse sand (1.435–1.500 mbsf), and then normal grading from very coarse–medium sand (1.360–1.435 mbsf). GSD shows increasingly poor sorting upward from 1.435 to 1.500 mbsf, and then a strong upward sorting trend from 1.360 to 1.435 mbsf.

4.1.2. Drill hole U1389A (seafloor–7.0 mbsf)

The sediments of the U1389A core mainly consist of calcareous mud (Figs. 2 and 3). Bioturbation is slight–moderate and shell fragments are present locally. The upper core (0.00–1.70 mbsf) comprises calcareous silty sand with an irregular basal contact. This layer contains scattered gastropods and shell fragments, and displays slight bioturbation (Figs. 2 and 3). The YSL, which is intercalated at 5.225–5.595 mbsf, is characterized by a calcareous silty sand layer, slight bioturbation, and

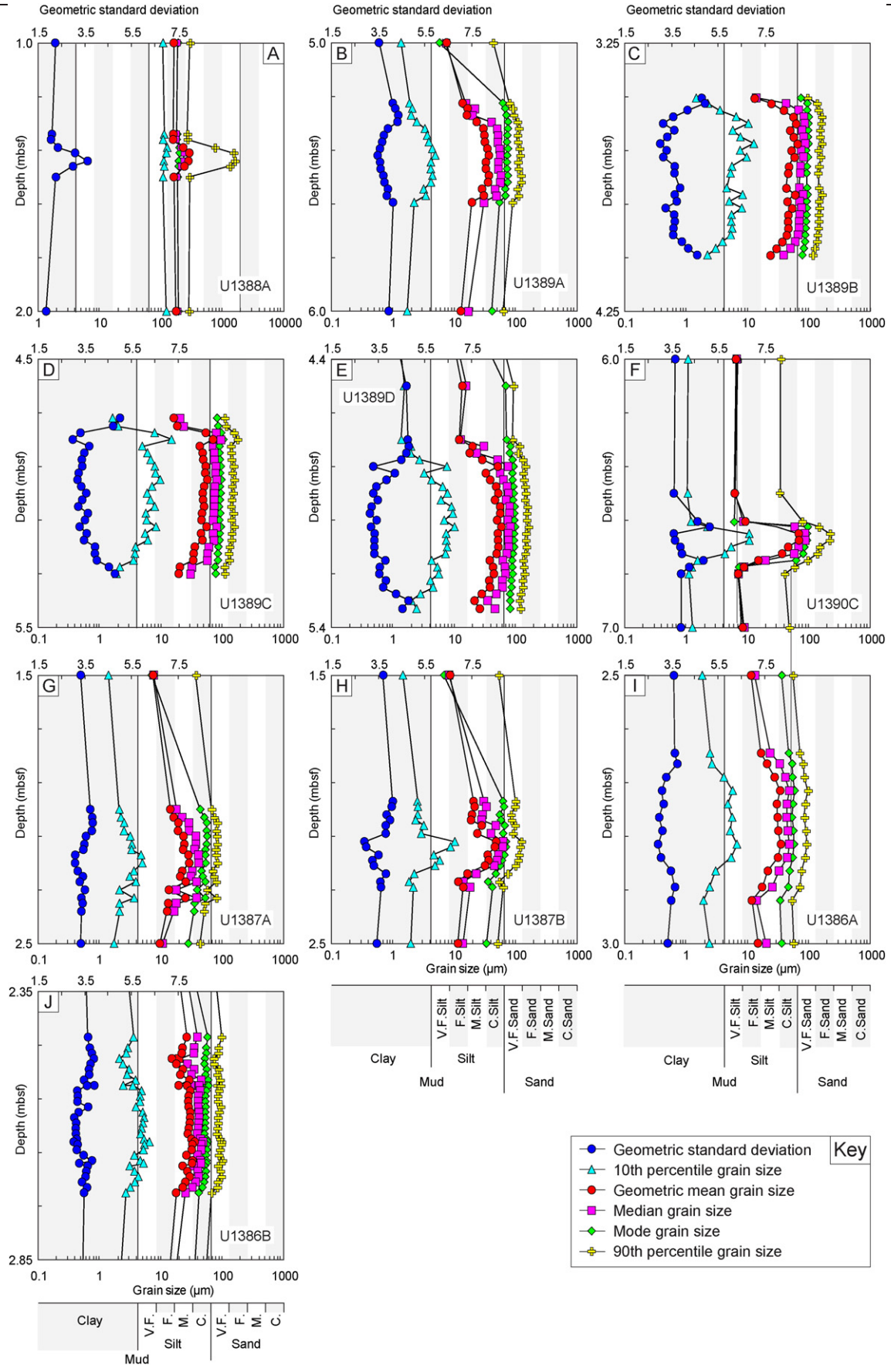

Fig. 4. Grain-size characteristics of the vertical variations observed in bi-gradational grading sequences.

rare shell fragments (Figs. 2 and 3). The YSL has gradational and bioturbated contacts at the top and base, respectively.

With regard to vertical variations in grain size characteristics (Fig. 4), the GM of the calcareous silty sand layer (5.225–5.595 mbsf) displays inverse grading from medium–coarse silt (5.495–5. 595 mbsf), and then normal grading from coarse–medium silt (5.320–5.225 mbsf). The other grain size characteristics (D_{10}, Md, Mo, and D_{90}) indicate a similar trend in vertical variations. However, the GSD of the calcareous silty sand layer shows an opposite trend in average grain size, with an increasingly well sorted trend upward from 5.420 to 5.595 mbsf, and then a poor upward sorting trend from 5.225 to 5.420 mbsf.

4.1.3. Drill hole U1389B (seafloor–5.0 mbsf)

The sediments of the U1389B core mainly consist of calcareous mud and calcareous silty mud (Figs. 2 and 3). Bioturbation is sparse–slight and shell fragments are present locally. The upper core (0.00–0.90 mbsf) comprises calcareous silty sand with a bioturbated basal contact (Figs. 2 and 3). The calcareous silty sand layer is intercalated by the YSL, located at 3.448–3.998 mbsf, and showing slight bioturbation and rare shell fragments (Figs. 2 and 3). This YSL shows gradational contacts at the top and base.

With regard to vertical variations in grain size characteristics (Fig. 4), the GM of the calcareous silty sand layer (3.448–3.998 mbsf) displays inverse grading from medium–coarse silt (3.815–3.998 mbsf), and then normal grading from coarse–very fine silt (3.448–3.550 mbsf). The other grain size characteristics (D_{10}, Md, Mo, and D_{90}) indicate a similar trend in vertical variations. However, the GSD of the calcareous silty sand layer shows an opposite trend in average grain size, with an increasingly well sorted trend upward from 3.998 to 3.865 mbsf, and then a poor upward sorting trend from 3.550 to 3.448 mbsf.

4.1.4. Drill hole U1389C (seafloor −8.0 mbsf)

The sediments of the U1389C core mainly consist of silty mud with biogenic carbonate, calcareous mud, and calcareous silty mud (Figs. 2 and 3). Bioturbation is slight and a few shell fragments are present locally. The upper core (0.00–0.51 mbsf) comprises calcareous silty sand with a gradational basal contact (Figs. 2 and 3). Two calcareous silty sand layers, the YSL and second sand layer (SSL), are intercalated at 4.720–5.300 mbsf and 7.09–7.28, respectively. Both sand layers show slight bioturbation, few shell fragments (Figs. 2 and 3), and gradational contacts at the top and base.

With regard to vertical variations in grain size characteristics (Fig. 4), the GM of the calcareous silty sand layer (4.720–5.300 mbsf) displays inverse grading from medium–coarse silt (5.125–5.300 mbsf), and then normal grading from very fine sand–medium silt (4.720–4.800 mbsf). The other grain size characteristics (D_{10}, Md, Mo, and D_{90}) indicate a similar trend in vertical variations. However, the GSD of the calcareous silty sand layer shows an opposite trend in average grain size, with an increasingly well sorted trend upward from 5.125 to 5.300 mbsf, and then a poor upward sorting trend from 4.720 to 4.800 mbsf.

4.1.5. Drill hole U1389D (seafloor–8.0 mbsf)

The sediments of the U1389D core mainly consist of calcareous silty mud and calcareous mud (Figs. 2 and 3). Bioturbation is sparse–slight and rare scaphopod fragments and few/rare shell fragments are present locally. The upper core (0.00–1.95 mbsf) comprises calcareous silty sand with a gradational basal contact (Figs. 2 and 3). Two calcareous silty sand layers (YSL and SSL) are intercalated at 4.700–5.330 mbsf and 6.640–6.870 mbsf, respectively. These two layers show bioturbated contacts at the top and base (Figs. 2 and 3). Bioturbation is absent in the upper sand bed and sparse in the lower sand bed. Shell fragments are rare in the basal part of the upper sand bed and few in the lower sandbed.

With regard to vertical variations in grain size characteristics (Fig. 4), the GM of the calcareous silty sand layer (4.700–5.330 mbsf) displays inverse grading from medium–coarse silt (5.125–5.330 mbsf), and then normal grading from coarse–fine silt (4.700–4.900 mbsf). The other grain size characteristics (D_{10}, Md, Mo, and D_{90}) indicate a similar trend in vertical variations. However, the GSD of the calcareous silty sand layer shows an opposite trend in average grain size, with an increasingly well sorted trend upward from 5.125 to 5.330 mbsf, and then a poor upward sorting trend from 4.700 to 4.900 mbsf.

4.1.6. Drill hole U1390B (seafloor–8.5 mbsf)

The sediments of the U1390B core mainly consist of calcareous mud (Figs. 2 and 3). Bioturbation is sparse–slight and shell fragments are few–rare. The YSL, which is intercalated at 6.63–6.75 mbsf, is characterized by sandy mud with biogenic carbonate layers, slight bioturbation, and few shell fragments (Figs. 2 and 3). This sand layer shows a bioturbated contact at the top and an erosional contact at the base.

4.1.7. Drill hole U1390C (seafloor–8.0 mbsf)

The sediments of the U1390C core mainly consist of mud with biogenic carbonates, calcareous mud, and silty mud with biogenic carbonates (Figs. 2 and 3). Bioturbation is slight and shell fragments are absent. The YSL, which is intercalated at 6.625–6.800 mbsf, is characterized by silty sand with biogenic carbonate layers, slight bioturbation, and few shell fragments (Figs. 2 and 3). The YSL shows a gradational contact at the top and base.

With regard to vertical variations in grain size characteristics (Fig. 4), the GM of the silty sand with biogenic carbonate layers (6.625–6.800 mbsf) displays inverse grading from very fine silt–very fine sand (6.675–6.800 mbsf), and then normal grading from very fine sand–very fine silt (6.625–6.665 mbsf). The other grain size characteristics (D_{10}, Md, Mo, and D_{90}) indicate a similar trend in vertical variations. However, the GSD of the silty sand with biogenic carbonate layers shows an opposite trend in average grain size, with poor upward sorting in the basal zone, from 6.750–6.800 mbsf. The GSD of the 6.650–6.750 mbsf interval shows increasingly well sorted material upwards, and then a poor upward sorting trend from 6.605 to 6.650 mbsf.

4.1.8. Drill hole U1387A (seafloor–5.0 mbsf)

The sediments of the U1387A core mainly consist of silty mud with biogenic carbonates (Figs. 2 and 3). Few–common shell fragments are present locally and bioturbation is sparse–slight. The upper core (0.00–0.20 mbsf) consists mainly of sandy silt with biogenic carbonates with a bioturbated basal contact (Figs. 2 and 3). The YSL, which is intercalated at 2.000–2.375 mbsf, is characterized by silty sand with biogenic carbonate layers (Figs. 2 and 3), sparse bioturbation, and common shell fragments. This YSL has a bioturbated contact at the top and base.

With regard to vertical variations in grain size characteristics (Fig. 4), the GM of the silty sand with biogenic carbonate layers (2.000–2.375 mbsf) displays inverse grading from fine–medium silt (2.220–2.375 mbsf), and then normal grading from medium–fine silt (2.000–2.220 mbsf). The other grain size characteristics (D_{10}, Md, Mo, and D_{90}) indicate a similar trend in vertical variations. However, the GSD of the silty sand with biogenic carbonate layers shows an opposite trend in average grain size, with an increasingly well sorted trend upward from 2.375 to 2.200 mbsf, and then a poor upward sorting trend from 2.000 to 2.200 mbsf.

4.1.9. Drill hole U1387B (seafloor–5.0 mbsf)

The sediments of the U1387B core mainly consist of silty mud, silty mud with biogenic carbonates, and nannofossil mud (Figs. 2 and 3). Few–rare shell fragments are present and bioturbation is sparse–slight. The upper core (0.00–0.52 mbsf) mainly consists of sandy silt with biogenic carbonates and has a bioturbated basal contact (Figs. 2 and 3). The YSL, which is intercalated at 1.970–2.290 mbsf, is characterized by silty sand with a biogenic carbonate layer (Figs. 2 and 3), slight bioturbation, and rare shell fragments. The YSL has a bioturbated contact at the top and base.

Table 3
Accelerator mass spectrometry (AMS) radiocarbon dating.

Laboratory code	Sample Name	Top (mbsf)	Conventional radiocarbon age (BP)	Local reservoir correction (years)	Dating material	Median probability (Calender year BP)	2 Sigma range (Calender year BP)		Calibration dataset
							Start	End	
Beta-340,176	U1389C1H4-23_25	4.730	11420 ± 40	400	Planktonic foraminifers (bulk)	12874	12727	13018	Marine13
Beta-371,500	U1389C1H4-27.5_30	4.775	12950 ± 50	400	Planktonic foraminifers (bulk)	14857	14470	15126	Marine13
Beta-340,177	U1389C1H4-50_52.5	5.000	11900 ± 40	400	Planktonic foraminifers (bulk)	13358	13256	13464	Marine13
Beta-369,963	U1389C1H4-72.5_75	5.225	14550 ± 60	400	Planktonic foraminifers (bulk)	17220	17001	17454	Marine13
Beta-369,964	U1389C1H4-77.5_80	5.275	14110 ± 50	400	Planktonic foraminifers (bulk)	16538	16310	16796	Marine13
Beta-340,178	U1389C1H4-80_82	5.300	9590 ± 40	400	Planktonic foraminifers (bulk)	10469	10317	10584	Marine13
SacA33894	U1390B1H4-146_148	5.960	9220 ± 35	400	Planktonic foraminifers (bulk except deep-dwelling species)	10040	9902	10154	Marine13
SacA33896	U1390B1H6-26_28	7.760	10360 ± 45	400	Planktonic foraminifers (bulk except deep-dwelling species)	11393	11218	11677	Marine13
SacA33886	U1390C2H3-10_12	7.500	12425 ± 40	400	Planktonic foraminifers (bulk except deep-dwelling species)	13905	13772	14043	Marine13
Beta-399,611	U1387A1H2-87.5_89.5	2.375	12650 ± 40	400	Planktonic foraminifers (bulk)	14143	13983	14315	Marine13
Beta-399,610	U1386A1H2-142_144	2.920	12150 ± 40	400	Planktonic foraminifers (bulk)	13596	13128	13744	Marine13

With regard to vertical variations in grain size characteristics (Fig. 4), the GM of the silty sand with biogenic carbonate layers (1.970–2.290 mbsf) displays inverse grading from fine–coarse silt (2.155–2.290 mbsf), and then normal grading from coarse–medium silt (1.970–2.115 mbsf). The other grain size characteristics (D_{10}, Md, Mo and D_{90}) indicate a similar trend in vertical variations. However, the GSD of the silty sand with biogenic carbonate layers shows an opposite trend in average grain size, with an increasingly well sorted trend upward from 2.115 to 2.290 mbsf, and then a poor upward sorting trend from 1.970–2.115 mbsf.

4.1.10. Drill hole U1386A (seafloor–5.0 mbsf)

The sediments of the U1386A core mainly consist of calcareous ooze and nannofossil ooze with mud (Figs. 2 and 3). Bioturbation is sparse and shell fragments are rare. The upper core (0.00–0.15 mbsf) mainly consists of silty sand with calcareous ooze and a bioturbated basal contact (Figs. 2 and 3). The YSL, which is intercalated at 2.645–2.920 mbsf, is characterized by silty sand with a biogenic carbonate layer (Figs. 2 and 3), sparse bioturbation, and rare shell fragments. The YSL has a bioturbated contact at the top and an irregular contact at the base.

With regard to vertical variations in grain size characteristics (Fig. 4), the GM of the silty sand with biogenic carbonate layers (2.645–2.920 mbsf) displays inverse grading from fine–coarse silt (2.815–2.920 mbsf), and then normal grading from coarse–medium silt (2.645–2.715 mbsf). The other grain size characteristics (D_{10}, Md, Mo and D_{90}) indicate a similar trend in vertical variations. However, the GSD of the silty sand with biogenic carbonate layers shows an opposite trend in average grain size, with an increasingly well sorted trend upward from 2.815–2.920 mbsf, and then a poor upward sorting trend from 2.715–2.645 mbsf.

4.1.11. Drill hole U1386B (seafloor–5.0 mbsf)

The sediments of the U1386B core mainly consist of calcareous silty mud and nannofossil mud (Figs. 2 and 3). Bioturbation is sparse and shell fragments are rare. The upper core (0.00–0.70 mbsf) mainly consists of silty sand with calcareous ooze and a bioturbated basal contact (Figs. 2 and 3). The YSL, which is intercalated at 2.37–2.71 mbsf, is characterized by silty sand with a biogenic carbonate layer (Figs. 2 and 3), absent bioturbation, and rare shell fragments. The YSL has a bioturbated contact at the top and an irregular contact at the base.

With regard to vertical variations in grain size characteristics (Fig. 4), the GM of the silty sand with biogenic carbonate layers (2.475–2.725 mbsf) displays inverse grading from fine–medium silt (2.615–2.725 mbsf), and then normal grading from medium–fine silt (2.475–2.515 mbsf). The other grain size characteristics (D_{10}, Md, Mo and D_{90}) indicate a similar trend in vertical variations. However, the GSD of the silty sand with biogenic carbonate layers shows an opposite trend in average grain size, with an increasingly well sorted trend upward from 2.630–2.725 mbsf, and then a poor upward sorting trend from 2.475–2.535 mbsf.

4.2. Radiocarbon dating

For drill hole U1389C (4.720–5.300 mbsf), radiocarbon ages were taken for six intervals within the calcareous silty sand layer. The results indicate a succession of random age values from the base to top of the layer (Fig. 2; Table 3). After applying the local reservoir correction (400 years), the ages are 12,874 cal. yr. BP (4.730 mbsf), 14,857 cal. yr. BP (4.775 mbsf), 13,358 cal. yr. BP (5.000 mbsf), 17,220 cal. yr. (5.225 mbsf), 16,538 cal. yr. (5.275 mbsf), and 10,469 cal. yr. (5.300 mbsf). The youngest calibrated age, 10,469 cal. yr. BP, was for the basal part (5.300 mbsf).

For drill hole U1390B (0.100–7.760 mbsf) radiocarbon ages were taken at two intervals of the core (Fig. 2; Table 3). After applying the local reservoir correction, the ages obtained ages are 10,040 cal. yr. BP (5.960 mbsf) and 11,393 cal. yr. BP (7.760 mbsf).

After applying the local reservoir correction, the radiocarbon ages for the 7.500 mbsf interval of drill hole U1390C, 2.375 mbsf interval of drill hole U1387A, and 2.920 mbsf interval of drill hole U1386A are 13,905 cal. yr. BP, 14,143 cal. yr. BP, and 13,596 cal. yr. BP, respectively.

4.3. Ichnological analysis

In general, discrete trace fossils with well-defined outlines are scarce and difficult to observe. Only *Thalassinoides*-like and *Ophiomorpha*-like structures (circular–subcircular sections, 6–12 mm wide and 3–13 mm high, along with approximately cylindrical structures 16–40 mm in length) are differentiated. However, ichnological analysis reveals a localized mottled background reflecting three intervals of biodeformational structures (but with no distinct outlines) in the sediments from the four cores of site U1389 (Fig. 5).

4.3.1. Interval A

Interval A is the thickest interval in any of the studied cores (41.5–51.5 cm). The sediments are homogeneous sands and neither discrete trace fossils nor mottled background is observed. Interval A is well developed in drill holes B, C, and D (Fig. 5). In drill hole A, this interval less homogenous and exhibits characteristics of both intervals A and B.

4.3.2. Interval B

Interval B corresponds to the units above and below interval A. It has a variable thickness of 7.5–30.5 cm, and consists of a well-developed

Fig. 5. Ichnological facies for each core taken at site U1389.

mottled background in which sediment mixing is evident. In some cases, discrete traces (*Thalassinoides*-like or *Ophiomorpha*-like) are recognized (Fig. 5). Using the Ichnological Digital Analysis Image Package (Dorador et al., 2014a), the percentage of trace fossils in the mottled background is variable, but is usually ~11% to 23%.

4.3.3. Interval C

Interval C is located above the upper boundary of Interval B. This near-homogenous interval ranges in thickness from 6.5 to 23 cm and neither traces nor a well-developed mottled background is observed. Interval C is similar to interval A, but with a higher mud component.

5. Discussion

5.1. Depositional models of bi-gradational graded contourite sequences

The standard contourite facies model (Faugères et al., 1984; Gonthier et al., 1984) was derived from the Faro Drift, located within the middle slope of the Gulf of Cádiz. The model recognizes a cyclic trend composed of three main facies: 1) homogeneous mud; 2) mottled silt and mud, and; 3) sand and silt. These facies are typically arranged in a coarsening-up to fining-up cycle that defines standard bi-gradational contourite sequences. Stow et al. (2002) presented a modified standard sequence that includes five principal divisions (C1–C5), while Stow and Faugères (2008) proposed a model for partial sequences, which are equally or more common than full bi-gradational sequences. From the bottom to top of a sequence, the five divisions of the modified standard sequence are mud (C1), mottled silt and mud (C2), sandy silt (C3), mottled silt and mud (C4), and mud (C5). This model represents an increase from weak to strong bottom current flow (the negatively graded sediments), and then back to weak current flow (the positively graded sediments).

The YSL identified in the cores from drill holes U1389A–D, U1390C, U1387A and B, and U1386A and B have similar grain size variations to those described in the bi-gradational contourite facies of Gonthier et al. (1984); Faugères et al. (1984), and Stow and Faugères (2008). In addition, vertical variation in the sorting of these sequences (Fig. 4) shows two distinct parts: a lower upward-well-sorted part and upper upward-poorly-sorted part. At the base of the bi-gradational sequence, the coarse fraction gradually increases with the acceleration of the bottom current. Our results show that grain size and degree of sorting are correlated (Fig. 6). At the maximum current velocity sediments are

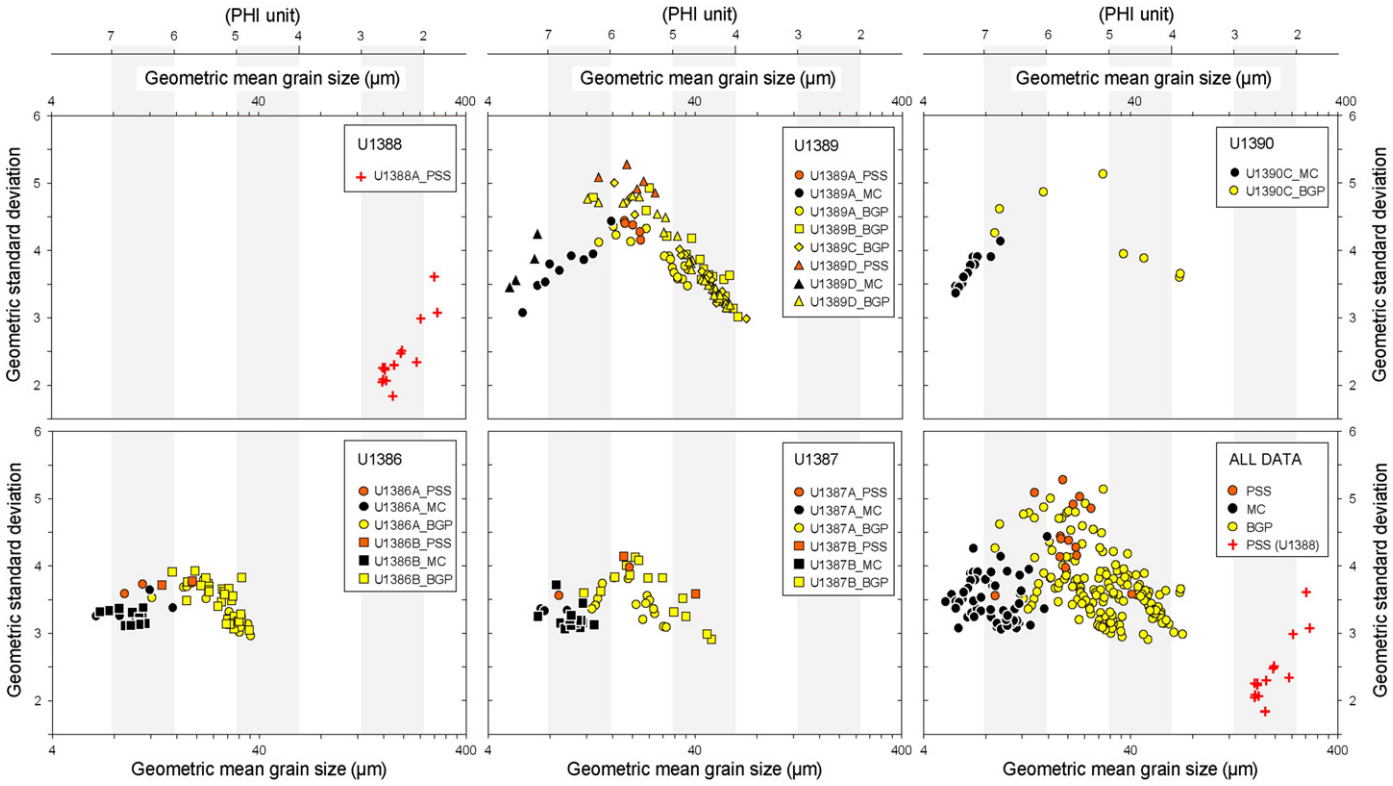

Fig. 6. Geometric grain sizes as a function of geometric standard deviation. Abbreviations are as follows: PSS = present-day seafloor sand; MC = muddy contourite; BGP = bi-gradational graded part.

well sorted (Fig. 4) and the grain size distribution shows a sharp peak in the coarser fraction (Fig. 3). In contrast, grain size sorting above the bi-gradational sequence shifts from well to poorly sorted with a weakening bottom current (Figs. 3 and 4).

Prior to the radiocarbon dating performed in this study, three different age models to describe the formation of the bi-gradational contourite sequence had been proposed (Fig. 7): Models 1 and 2 assume that the base and top intervals of the sequences show different ages ($\Delta T \neq 0$), suggesting continuous accumulation over a relatively long duration. In model 1, a smooth radiocarbon dating curve results from the continuous accumulation of marine snow (pelagic/hemipelagic deposits) consisting of dead or dying plankton and inorganic wind dust. In model 2, an irregular radiocarbon dating curve results from sand layers consisting of reworked older material and not just pelagic deposits. Model 3 assumes that both the top and basal horizons are of similar age ($\Delta T = 0$). This model is based on rapid deposition from a gravity

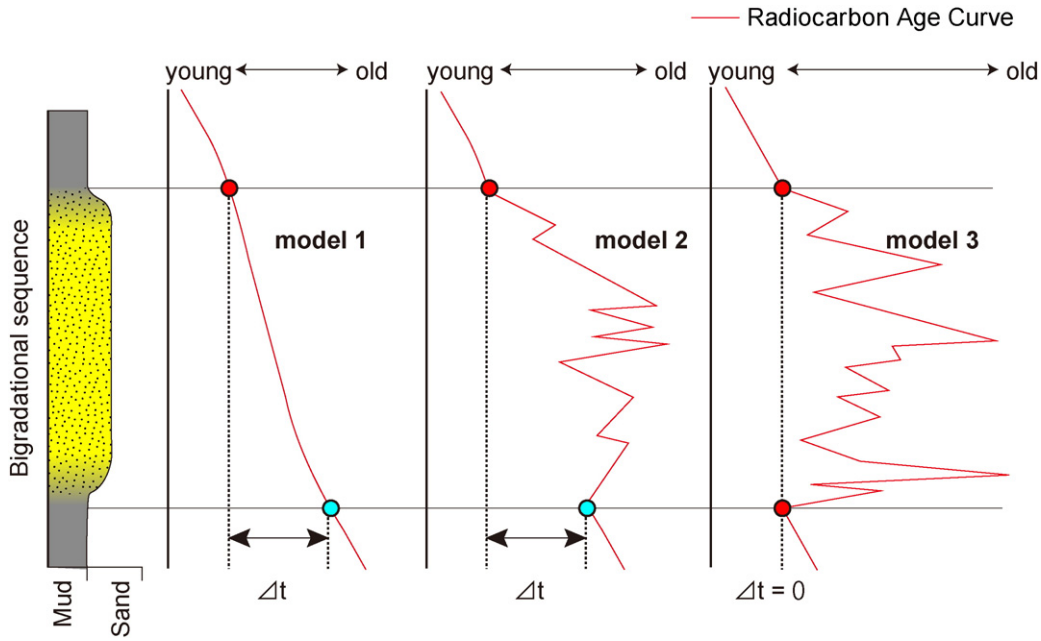

Fig. 7. Schematic radiocarbon age models for bi-gradational grading.

flow (in the form of a turbidity current), benthic storm, or other catastrophic event. We use the high-resolution radiocarbon dates from drill hole U1389C to test these models of bi-gradational contourite sequence formation.

For the YSL of drill hole U1389C, the radiocarbon ages show an irregular curve between the top and basal horizons. This indicates that the sandy part of the bi-gradational grading consists of reworked materials on bottom current pathways and models 1 does not apply to this sequence. The radiocarbon age of the basal interval is ~10 cal. yr. BP (Table 3). On the other hand, the top of the sequence is no younger (Fig. 2 and Table 3) and, therefore, using radiocarbon dating alone it is difficult to determine whether model 2 or 3 is more appropriate. However, ichnological data can also provide information regarding the duration of deposition (Fig. 5).

For drill hole U1390C, the YSL sequence includes three intervals. At the base, Interval A is characterized by a relatively sharp lower boundary and an absence of bioturbational features, suggesting rapid deposition with no time for tracemaker activity. Most likely, this interval reflects the rapid deposition of coarse sediments during a single high sedimentation rate event. Nevertheless, it is also possible that environmental conditions may cause the absence of bioturbational structures; for example, low rates of oxygenation or stressful conditions such as high current velocities. Interval B is characterized by a well-developed mottled background and discrete trace fossils. It likely reflects a diminution of the sedimentation rate, which facilitates bioturbation by tracemakers. The interval also contains a variable percentage of trace fossil bioturbation that likely reflects differences in the rate of sedimentation. The mottled background reflects the burrowing activity of tracemakers on the sea-floor or just below, suggesting a soupy or soft-ground sediment mixture. Finally, Interval C reveals a return to high sedimentation rates and lower levels of bioturbation. In this case, the increase in sedimentation is likely due to mud deposition. If these increased sedimentation rates account for the absence of bioturbational features, then model 3 provides the best fit to the bi-gradational sequence of the YSL. However, while the ichnological results are useful for determining the onset of the sandy interval, future studies that include further radiocarbon data and the integration of other analyses and proxies are required to fully characterize this system.

5.2. Spatial variations in the Gulf of Cádiz CDS

The YSLs identified in this study correlate the holes in the sites and are characterized by bi-gradational sequence of facies (Fig. 2). The YSL of U1389A–D, U1387A and B, and U1386 A and B are coeval. On the basis of radiocarbon dating, we identified YSL layers from three main periods: (1) the Boreal chronozone, (2) the Younger Dryas, and (3) the Bølling-Allerød.

The Boreal chronozone occurred between ~10,770–10,700 and 8900 cal. yr. BP (Mangerud et al., 1974; Sirviö and Kajander, 2003; Bos et al., 2007). The YSL identified in drill holes U1389A–D are slightly younger than 10,469 cal. yr. BP and do not correlate with other sand layers in other sites (U1390, U1387, and U1386).

The Younger Dryas occurred between ~13,000 and 11,500 years BP (Mangerud et al., 1974; Alley et al., 1993; Meese et al., 1997; Bard, 1998; Alley, 2000; Kennett et al., 2009). The ages of the YSL in site U1390 are between 13,905 and 11,393 cal. yr. BP. The top contact of the YSL in U1390B is intercalated 20 cm below the 11,393 cal. yr. BP horizon, and 204 cm below the 10,040 cal. yr. BP horizon. The base contact of the YSL in U1390C is 75 cm above the 13,905 cal. yr. BP interval. For drill holes U1389C and U1389D, SSL are intercalated at 1.54 m and 1.84 m below the YSL, respectively. Although accurate radiocarbon ages for the SSL were not measured in this study, their horizons were correlated to the YSL of U1390C, which was emplaced during the Younger Dryas or before (Fig. 2). Both the SSL of U1389 and YSL of U1390 are ~1.54–2.04 m below the ~10,469 cal. yr. BP horizon. On this basis, we tentatively conclude that these layers are coeval (Fig. 2).

The Bølling-Allerød occurred 14,500–12,800 years BP (Mangerud et al., 1974; Liu et al., 2009). The ages of the YSL in U1387 and U1386 are slightly less than 14,143 cal. yr. BP and 13,596 cal. yr. BP, respectively, and it is likely that they correlate with each other.

The regional distribution of YSL and SSL indicates that sand layer deposition in the Gulf of Cádiz CDS was not uniform. The bi-gradational YSL sequences from the beginning of the Boreal chronozone are observed in the central CDS (site U1389). The YSL in drill hole U1389C indicates a random age order within the sequence (Fig. 2; Table 3). The youngest age (10,469 cal. yr. BP) is recorded in the basal interval (5.300 mbsf). Nevertheless, the sandy parts of the YSL (above 5.300 mbsf) are older, with ages of 16,538, 17,220, 13,358, 14,857, and 12,874 cal. yr. BP from the bottom to the top of the YSL. This observation is explained by the erosion of sandy materials from a comparatively upstream area. Our observations suggest that deposition was associated with the ML, but not with the MU. Sedimentological and ichnological analyses show that the sandy deposits mainly consist of reworked materials that show older radiocarbon ages and rapid deposition. These results indicate that the deposition and reworking of the sand occurred locally. The sediment source area was probably proximal (near the site U1388 or the Gibraltar Strait) and may have been a sandy sheeted drift identified close to Strait of Gibraltar (Hernández-Molina et al., 2014a).

The bi-gradational sequence of facies intercalated in the sediments of the Younger Dryas is also identified only in the central CDS (sites U1389 and U1390). These sites are also influenced by ML and the source area of the sands could also be proximal (near to site U1388 or to the Gibraltar Strait).

The bi-gradational graded contourite developed at the Bølling-Allerød occurs in sites U1387 and U1386 of the Faro Drift, an area controlled by the MU. There are no coeval sand layers in U1389 and U1390, which indicates that the sandy materials in sites U1387 and U1386 were not transported from an area proximal to the Gulf of Cádiz CDS. Possible causes of the bi-gradational sequences in U1387 and U1386 include sudden gravity-controlled geological events such as turbidity currents triggered by earthquake-induced tsunami, submarine landslides, or meteorite impact. There is no geological and topographical evidence for large scale submarine landslides such as Storegga Slide with >2000 km^2 in offshore Norway induced by large earthquake had occurred large tsunami at ca. 7.9 cal. Ky BP (Dawson et al., 1988; Smith et al., 2004), or meteorite impacts in this area during the period of interest. However, the southern Iberian margin is seismically active due to the convergent plate boundary between Eurasia (Iberian sub-plate) and Africa (Nubian sub-plate; Zitellini et al., 2009). A number of earthquake-induced tsunami events of historical or prehistorical age are recorded in the sediments of offshore Portugal or in the coastal lowland area of the Gulf of Cádiz (e.g., Lario et al., 2011; Rodríguez-Vidal et al., 2011). It is possible that the trigger of the bi-gradational graded sequences of the muddy contourite succession may be related to an earthquake or its related tsunami.

5.3. Trigger events processes of formation in the CDS

In general, tsunamis consist of a wave or series of waves with long wavelengths and periods, caused by an abrupt vertical displacement of the ocean bottom, usually due to earthquakes, landslides, or other external agents, for example volcanic eruptions or meteorite impacts (Shanmugam, 2006b, 2012). Tsunami waves carry energy through the water but do not displace the water horizontally, nor do they transport sediment. However, during the transformation stage tsunami waves erode and incorporate sediment into the incoming wave. Tsunami-related traction currents can thus transport large concentrations of sediment in suspension (Shanmugam, 2006b, 2012; Abrantes et al., 2008). Tsunamis are also important mechanisms for triggering sediment failures, as the advancing tsunami wave front can generate large hydrodynamic pressures on the seafloor, thereby overwhelming the slope stability factors (Wright and Rathje, 2003). A case study on the 2011

Tohoku-oki tsunami recognized possible submarine tsunami deposits on the outer shelf of Sendai Bay, Japan and indicated that large tsunamis can generate turbidity currents (Ikehara et al., 2014). Re-suspended muddy shelf sediments generated by the high frictional velocities that occur when tsunami waves propagate into shallow shelf waters (Sugawara and Goto, 2012) create a water column with a high concentration of suspended sediment. Re-suspension of diatomaceous surface sediments also occurs by strong ground shaking associated with earthquakes and the agitation by subsequent tsunami waves. The collapse of the water column generates repeated turbidity currents on the outer shelf. Other study conducted by Niitani et al. (2013) also showed that tsunami-induced gravity currents generated in an experimental flume. In their study, a sediment-gravity flow which occurred at the lower foreshore to the upper shoreface by tsunamigenic oscillatory flows in the experimental flume was obviously reconstructed. However, questions about the generation, growth, and transport mechanisms of submarine tsunami-related sediments remain debated.

The most famous historic earthquake-induced tsunami of the southern Iberian margin is the 1755 Lisbon tsunami (Baptista et al., 2003), which appears in the geological record from Portugal to the Gibraltar Strait (e.g., Dawson et al., 1991, 1988; Hindson et al., 1996; Dabrio et al., 1998, 2000; Hindson and Andrade, 1999; Luque et al., 1999, 2001, 2004; Luque, 2002; Whelan and Kelletat, 2005; Gracia et al., 2006; Viana-Baptista et al., 2006; Cuven et al., 2013). Gràcia et al. (2010) also recognized 6 Holocene turbidite events as seismically triggered and estimated ~1800 years as a recurrence period for large earthquakes (Mw 8.0). Morales et al. (2008) identified five tsunami deposits of 1600 years or younger in the laterally continuous shelly layers of low-energy environments from the Huelva Estuary. The Holocene paleo-tsunami catalogue of southwestern Iberia (Lario et al., 2011) includes at least five tsunami events generated by strong earthquakes during the last 7000 years and estimates a recurrence interval of 1500–2000 years for large tsunami events. Koster and Reicherter (2014) also reported an ~4000 year-old tsunami deposit preserved in Holocene coastal cliffs of Barbate and Zahara de los Atunes, southern Spain.

Although there is evidence for Holocene tsunami events in the Gulf of Cádiz and its coastal lowlands, our cores show no evidence for such events after the beginning of the Boreal (Fig. 2). This suggests that: 1) after the beginning of the Boreal, seismic- or tsunami-generated coarse sediment transportation from coastal areas of the Gulf of Cádiz to the offshore and deeper seafloor did not affected the grain size of bottom sediments, or; 2) an intense bottom current (MU) may have merged with turbidity currents to widely rework coarse materials. Llave et al. (2006) also found out that the coarser contourite deposits on the central area of the middle slope of the Gulf of Cádiz are mostly associated with the Last Glacial Maximum, the Younger Dryas, and Heinrich events. Using grain size as a proxy for the MOW, they advocate that an enhancement of the ML (the lower MOW branch) during climatic cooling and stronger MU (upper MOW branch) circulation occurred during warm intervals. The spatial distribution of sandy contourites was controlled by variations in bathymetric position and current strength of the MOW (Llave et al., 2006).

The results of this study indicate three bi-gradational sequences in the Gulf of Cádiz CDS. These were deposited at the Bølling-Allerød (~13–14 cal. Ky BP), the Younger Dryas (~12–13 cal. Ky BP), and the beginning of Boreal (~10 cal. Ky BP). The recurrence interval of these events is ~1–2 Ky, the same range as for historic and pre-historic tsunami records (e.g., Morales et al., 2008; Gràcia et al., 2010; Lario et al., 2011; Koster and Reicherter, 2014). This implies that the three YSLs are probably related with large tsunami events occurred around the Cádiz CDS. Our results also suggest that during the Bølling-Allerød, the Younger Dryas, and the early Boreal, an enhanced bottom current (ML) occurred in the deep waters of the Gulf of Cádiz. In contrast, the MU became weaker along the shallower seafloor in the Gulf of Cádiz. As a result of this situation, downslope processes on the seafloor were controlled by the ML. The development of bi-gradational graded contourite on the middle slope (sites U1387 and U1386) during the Bølling-Allerød may indicate a transitional condition between enhanced ML (during cool climate) and a stronger MU (warm condition). This model of bi-gradational graded contourite formation in the Gulf of Cádiz explains why no similar bi-gradational sequences are found above the beginning of the Boreal horizon.

In this discussion, we could not exhibit direct evidences of "tsunami" from the sand layers but only we obtained circumstantial evidences. Nevertheless, we consider that our ideas were still important for the future research on contourite. Because studies of contourite which almost composed of reworked materials need various approaches to understand origins, natures, and transport processes. We hope that our speculations will be validated by other approaches and scientists.

6. Conclusions

Younger Sand Layers (YSLs) are intercalated within a Late Pleistocene to Early Holocene muddy contourite succession in the Gulf of Cádiz. In this study, we characterized the YSL using sedimentological and ichnological observations, as well as AMS ^{14}C dating. On the basis of our results, the main conclusions of this study are: 1) YSLs are characterized by bi-gradational sequences, which exhibit vertical changes both in grain size and in sorting; 2) The YSL formed during three different ages intervals including the Bølling-Allerød (sites U1387 and U1386), the Younger Dryas (site U1390), and the beginning of the Boreal (site U1389); 3) The genesis of YSL varies. The sequences in the beginning of Boreal (U1389C) likely represent a bottom current reworked deposit with high sedimentation rate; 4) The results of sedimentological analyses, ichnological treatment, spatial distributions, and radiocarbon dating of the YSLs in this study suggest that the YSLs are formed from tsunami-related bottom current and consist of reworked materials. However the source area of sandy sediments is unclear, although our results show it to be variable and area dependent. Some sandy deposits are transported from proximal sectors of the CDS (close to the Strait of Gibraltar) by the MOW; however, in other cases local gravity flows resulting from instability on the adjacent margin could provide the sandy material.

Acknowledgments

This research used samples and data collected through the Integrated Ocean Drilling Program (IODP) and was supported by IODP After Cruise Research Program, JAMSTEC. We thank Dr. Kuroda (JAMSTEC) and anonymous reviewer who provided constructive comments and helpful suggestions. We also thank the Bremen Core Repository team for their support during the Onshore Science Party. This research was supported through the Ciencia y Tecnologías Marinas projects CTM 2008-06399-C04/MAR and CTM 2012-39599-C03. Research of R-T and JD was financed by Project CGL2012-33281 supported through project funded by the Spanish Ministry of Economy and Competitiveness. The Research Group RNM-178 (Junta de Andalucía), and a pre-doctoral grant supported by the University of Granada, and the Continental Margins Research Group at Royal Holloway University of London (UK) also contributed to the research. We acknowledge the French Artemis program of the Institut National des Sciences de l'Univers for AMS ^{14}C datings and would like to thank Editage (www.editage.jp) for the English language editing.

Appendix A. Supplementary data

Supplementary data associated with this article can be found in the online version, at doi: http://dx.doi.org/10.1016/j.margeo.2015.09.009. These data include the Google map of the most important areas described in this article.

References

Abrantes, F., Alt-Epping, U., Lebreiro, S., Voelker, A., Schneider, R., 2008. Sedimentological record of tsunamis on shallow-shelf areas: the case of the 1969 AD and 1755 AD tsunamis on the Portuguese shelf off Lisbon. Mar. Geol. 249, 283–293. http://dx.doi.org/10.1016/j.margeo.2007.12.004.

Alley, R.B., 2000. The Younger Dryas cold interval as viewed from central Greenland. Quat. Sci. Rev. 19, 213–226. http://dx.doi.org/10.1016/S0277-3791(99)00062-1.

Alley, R.B., Meese, D.A., Shuman, C.A., Gow, A.J., Taylor, K.C., Grootes, P.M., Whiteparallel, J.W.C., Ram, M., Waddington, E.D., Mayewski, P.A., Zielinski, G.A., 1993. Abrupt increase in Greenland snow accumulation at the end of the Younger Dryas event. Nature 362, 527–529. http://dx.doi.org/10.1038/362527a0.

Bard, E., 1998. Geochemical and geophysical implications of the radiocarbon calibration. Geochim. Cosmochim. Acta 62, 2025–2038. http://dx.doi.org/10.1016/S0016-7037(98)00130-6.

Bahr, A., Jiménez-Espejo, F., Kolasinac, N., Grunert, P., Hernández-Molina, F.J., Röhl, U., Voelker, A., Escutia, C., Stow, D.A.V., Hodell, D., Alvarez-Zarikian, C.A., 2014. Deciphering bottom current strength and paleoclimate signals from contourite deposits in the Gulf of Cádiz during the last 140 kyr: an inorganic geochemical approach. Geochem. Geophys. Geosyst. 15, 3145–3160. http://dx.doi.org/10.1002/2014GC005356.

Baptista, M.A., Miranda, J.M., Chierici, F., Zitellini, N., 2003. New study of the 1755 earthquake source based on multi-channel seismic survey data and tsunami modeling. Nat. Hazards Earth Syst. Sci. 3, 333–340https://hal.archives-ouvertes.fr/hal-00299044.

Buforn, E., Bezzeghoud, M., Udías, A., Pro, C., 2004. Seismic sources on the Iberia-African Plate boundary and their tectonic implications. Pure Appl. Geophys. 161, 623–646. http://dx.doi.org/10.1007/s00024-003-2466-1.

Buforn, E., Sanz de Galdeano, C., Udías, A., 1995. Seismotectonics of the Ibero-Maghrebian region. Tectonophysics 248, 247–261. http://dx.doi.org/10.1016/0040-1951(94)00276-F.

Bos, J.A.A., van Geel, B., van der Plicht, J., Bohnche, S.J.P., 2007. Preboreal climate oscillations in Europe: Wiggle-match dating and synthesis of Dutch high-resolution multi-proxy records. Quat. Sci. Rev. 26, 1927–1950. http://dx.doi.org/10.1016/j.quascirev.2006.09.012.

Cuven, S., Paris, R., Falvard, S., Miot-Noirault, E., Benbakkar, M., Schneider, J.-L., Billy, I., 2013. High-resolution analysis of a tsunami deposit: case-study from the 1755 Lisbon tsunami in southwestern Spain. Mar. Geol. 337, 98–111. http://dx.doi.org/10.1016/j.margeo.2013.02.002.

Dabrio, C.J., Zazo, C., Goy, J.L., Sierro, F.J., Borja, F., Lario, J., Gonzáles, J.A., Flores, J.A., 2000. Depositional history of estuarine infill during the Last Postglacial transgression (Gulf of Cádiz, Southern Spain). Mar. Geol. 162, 381–404. http://dx.doi.org/10.1016/S0025-3227(99)00069-9.

Dabrio, C.J., Zazo, C., Lario, J., Goy, J.L., Sierro, F.J., Borja, F., González, J.A., Flores, J.A., 1998. Holocene incised-valley fills and coastal evolution in the Gulf of Cádiz (southern Spain). Mediterranean and Black Sea Subcommission Newsletter 20, pp. 45–48.

Dawson, A.G., Foster, I.D., Shi, S., Smith, D.E., Long, D., 1991. The identification of tsunami deposits in coastal sediment sequences. Sci. Tsunami Haz. 9, 73–82.

Dawson, A.G., Long, D., Smith, D.E., 1988. The Storegga slides: evidence from eastern Scotland for possible tsunami. Mar. Geol. 99, 265–287. http://dx.doi.org/10.1016/0025-3227(88)90146-6.

Dorador, J., Rodríguez-Tovar, F.J., 2014. A novel application of digital image treatment by quantitative pixels analysis to trace fossil research in marine cores. PALAIOS 24, 533–538.

Dorador, J., Rodríguez-Tovar, F.J., IODP Expedition 339 Scientists, 2014a. Quantitative estimation of bioturbation based on digital image analysis. Mar. Geol. 349, 55–60. http://dx.doi.org/10.1016/j.margeo.2014.01.003.

Dorador, J., Rodríguez-Tovar, F.J., IODP Expedition 339 Scientists, 2014b. Digital image treatment applied to ichnological analysis of marine core sediments. Facies 60, 39–44. http://dx.doi.org/10.1007/s10347-013-0383-z.

Duarte, J.C., Rosas, F.M., Terrinha, P., Gutscher, M.-A., Malavieille, J., Silva, S., Matias, L., 2011. Thrust–wrench interference tectonics in the Gulf of Cadiz (Africa–Iberia plate boundary in the North-East Atlantic): insights from analog models. Mar. Geol. 289, 135–149. http://dx.doi.org/10.1016/j.margeo.2011.09.014.

Expedition 339 Scientists, 2012. Mediterranean Outflow: Environmental Significance of the Mediterranean Outflow Water and its Global Implications. Integrated Ocean Drilling Program Expedition 339 Preliminary Report http://dx.doi.org/10.2204/iodp.pr.339.2012 (97 pp.).

Faugères, J.-C., Gonthier, E., Stow, D.A.V., 1984. Contourite drift moulded by deep Mediterranean outflow. Geology 12, 296–300. http://dx.doi.org/10.1130/0091-7613(1984)12<296:CDMBDM>2.0.CO;2.

García, M., Hernández-Molina, F.J., Llave, E., Stow, D.A.V., León, R., Fernández-Puga, M.C., Díaz del Río, V., Somoza, L., 2009. Contourite erosive features caused by the Mediterranean outflow water in the Gulf of Cádiz: Quaternary tectonic and oceanographic implications. Mar. Geol. 257, 24–40. http://dx.doi.org/10.1016/j.margeo.2008.10.009.

Gracia, F.J., Alonso, C., Benavente, J., Anfuso, G., Del Río, L., 2006. The different coastal records of the 1755 tsunami waves along the South Atlantic Spanish coast. Z. Geomorphol. Suppl. 146, 195–220.

Gràcia, E., Vizcaino, A., Escutia, C., Asioli, A., Rodés, A., Pallàs, R., Garcia-Orellana, J., Lebreiro, S., Goldfinger, C., 2010. Holocene earthquake record offshore Portugal (SW Iberia): testing turbidite paleoseismology in a slow-convergence margin. Quat. Sci. Rev. 29, 1156–1172. http://dx.doi.org/10.1016/j.quascirev.2010.01.010.

Gonthier, E.G., Faugères, J.C., Stow, D.A.V., 1984. Contourite Facies of the Faro Drift, Gulf of Cádiz. In: Stow, D.A.V., Piper, D.J.W. (Eds.), Fine-Grained Sediments: Deep Water Processes and Facies. Geological Society of London, Special Publication 15, pp. 275–292. http://dx.doi.org/10.1144/GSL.SP.1984.015.01.18.

Grimson, N.L., Chen, W.-P., 1986. The Azores–Gibraltar plate boundary: focal mechanisms, depths of earthquakes and their tectonic implications. J. Geophys. Res. 91 (B2), 2029–2047. http://dx.doi.org/10.1029/JB091iB02p02029.

Hernández-Molina, F.J., Llave, E., Preu, B., Ercilla, G., Fontan, A., Bruno, M., Serra, N., Gomiz, J.J., Brackenridge, R.E., Sierro, F.J., Stow, D.A.V., García, M., Juan, C., Sandoval, N., Arnaiz, A., 2014a. Contourite processes associated to the Mediterranean Outflow Water after its exit from the Gibraltar Strait: global and conceptual implications. Geology 42, 227–230. http://dx.doi.org/10.1130/G35083.1.

Hernández-Molina, F.J., Llave, E., Somoza, L., Fernández-Puga, M.C., Maestro, A., León, R., Barnolas, A., Medialdea, T., García, M., Vázquez, J.T., Díaz del Río, V., Fernández-Salas, L.M., Lobo, F., Alveirinho Dias, J.M., Rodero, J., Gardner, J., 2003. Looking for clues to paleoceanographic imprints: a diagnosis of the Gulf of Cadiz contourite depositional systems. Geology 31, 19–22. http://dx.doi.org/10.1130/0091-7613(2003)031<0019:LFCTPI>2.0.CO;2.

Hernández-Molina, F.J., Llave, E., Stow, D.A.V., García, M., Somoza, L., Vázquez, J.T., Lobo, F.J., Maestro, A., Díazdel Río, V., León, R., Medialde, T., Gardner, J., 2006. The contourite depositional system of the Gulf of Cádiz: a sedimentary model related to the bottom current activity of the Mediterranean outflow water and its interaction with the continental margin. Deep-Sea Res. II 53, 1420–1463. http://dx.doi.org/10.1016/j.dsr2.2006.04.016.

Hernández-Molina, F.J., Stow, D.A.V., Alvarez-Zarikian, C.A., Acton, G., Bahr, A., Balestra, B., Ducassou, E., Flood, R., Flores, J.-A., Furota, S., Grunert, P., Hodell, D., Jimenez-Espejo, F., Kim, J.K., Krissek, L., Kuroda, J., Li, B., Llave, E., Lofi, J., Lourens, L., Miller, M., Nanayama, F., Nishida, N., Richter, C., Roque, C., Pereira, H., Goñi, M.F.S., Sierro, F.J., Singh, A.D., Sloss, C., Takashimizu, Y., Tzanova, A., Voelker, A., Williams, T., Xuan, C., 2014b. Onset of Mediterranean outflow into the North Atlantic. Science 344, 1197–1316. http://dx.doi.org/10.1126/science.1251306.

Hernández-Molina, F.J., Stow, D.A.V., Alvarez-Zarikian, C., Expedition IODP 339 Scientists, 2013. IODP Expedition 339 in the Gulf of Cadiz and off West Iberia: decoding the environmental significance of the Mediterranean Outflow Water and its global influence. Sci. Drill. 16, 1–11. http://dx.doi.org/10.5194/sd-16-1-2013.

Hindson, R.A., Andrade, C., 1999. Sedimentation and hydrodynamic processes associated with the tsunami generated by the 1755 Lisbon earthquake. Quat. Int. 56, 27–38. http://dx.doi.org/10.1016/S1040-6182(98)00014-7.

Hindson, R.A., Andrade, C., Dawson, A.G., 1996. Sedimentary processes associated with the tsunami generated by the 1755 Lisbon Earthquake on the Algarve Coast, Portugal. Phys. Chem. Earth 21, 57–63. http://dx.doi.org/10.1016/S0079-1946(97)00010-4.

Hüneke, H., Stow, D.A.V., 2008. Identification of Ancient Contourites: Problems and Palaeoceanographic Significance. In: Rebesco, M., Camerlenghi, A. (Eds.), Contourites. Developments in Sedimentology 60, pp. 323–344.

Ikehara, K., Irino, T., Usami, K., Jenkins, R., Omura, A., Ashi, J., 2014. Possible submarine tsunami deposits on the outer shelf of Sendai Bay, Japan resulting from the 2011 earthquake and tsunami off the Pacific coast of Tohoku. Mar. Geol. 358, 120–127. http://dx.doi.org/10.1016/j.margeo.2014.01.001.

Kennett, D.J., Kennett, J.P., West, A., Mercer, C., Que Hee, S.S., Bement, L., Bunch, T.E., Sellers, M., Wolbach, W.S., 2009. Nanodiamonds in the Younger Dryas Boundary Sediment Layer. Science 323, 94. http://dx.doi.org/10.1126/science.1162819.

Koster, B., Reicherter, K., 2014. Sedimentological and geophysical properties of a ca. 4000 year old tsunami deposit in southern Spain. Sediment. Geol. 314, 1–6. http://dx.doi.org/10.1016/j.sedgeo.2014.09.006.

Lario, J., Zazo, C., Goy, J.L., Silva, P.G., Bardaji, T., Cabero, A., Dabrio, C.J., 2011. Holocene palaeotsunami catalogue of SW Iberia. Quat. Int. 242, 196–200. http://dx.doi.org/10.1016/j.quaint.2011.01.036.

Liu, Z., Otto-Bliesner, B.L., He, F., Brady, E.C., Tomas, R., Clark, P.U., Carlson, A.E., Lynch-Stieglitz, J., Curry, W., Brook, E., Erickson, D., Jacob, R., Kutzbach, J., Cheng, J., 2009. Transient simulation of Last Deglaciation with a new mechanism for Bølling-Allerød warming. Science 325, 310–314. http://dx.doi.org/10.1126/science.1171041.

Llave, E., Schonfeld, J., Herna'ndez-Molina, F.J., Mulder, T., Somoza, L., del Rio, V.D., Sanchez-Almazo, I., 2006. High-resolution stratigraphy of the Mediterranean outflow contourite system in the Gulf of Cadiz during the late Pleistocene: the impact of Heinrich events. Mar. Geol. 227, 241–262. http://dx.doi.org/10.1016/j.margeo.2005.11.015.

Luque, L., 2002. Cambios en los Paleoambientes Costeros del sur de la Península Ibérica (España) Durante el Holoceno (Tesis Doctoral) Universidad Complutense de Madrid.

Luque, L., Lario, J., Zazo, C., Goy, J.L., Dabrio, C.J., Silva, P.G., 2001. Tsunami deposits as palaeoseismic indicators: examples from the Spanish coast. Acta Geol. Hisp. 36, 197–211.

Luque, L., Zazo, C., Goy, J.L., Dabrio, C.J., Civis, J., Lario, J., Gómez-Ponce, C., 1999. Los depósitos del tsunami de Lisboa de 1755. Su registro en la Bahía de Cádiz: Flecha de Valdelagrana (Spain). Actas de la X Reunión Nacional del 152 Luis de Luque, RAMPAS, 10, 2008Revista Atlántica-Mediterránea de Prehistoria y Arqueología Social 10. Universidad de Cádiz Cuaternario, Girona, pp. 63–66 (2008, 131–153).

Luque, L., Zazo, C., Lario, J., Goy, J.L., Civis, J., González-Hernández, F.M., Silva, P.G., Dabrio, C.J., 2004. El efecto del tsunami del año 1755 en el Litoral de Conil de la Frontera (Cádiz). In: Baquedano, E., Rubio, S. (Eds.), Miscelanea en homenaje a Emiliano Aguirre. Geología 1. Comunidad de Madrid, Museo Arqueológico Regional, Madrid, pp. 72–82.

Mangerud, J., Andersen, S.T., Berglund, B.E., Donner, J.J., 1974. Quaternary stratigraphy of Norden, a proposal for terminology and classification. Boreas 3, 109–128. http://dx.doi.org/10.1111/j.1502-3885.1974.tb00669.x.

Martín-Chivelet, J., Fregenal Martínez, M.A., Chacón, B., 2008. Traction Structures in Contourites. In: Rebesco, E., Camerlenghi, A. (Eds.), Contourites. Elsevier, Amsterdam, pp. 159–181.

Meese, D.A., Gow, A.J., Alley, R.B., Zielinski, G.A., Grootes, P.M., Ram, M., Taylor, K.C., Mayewski, P.A., Bolzan, J.F., 1997. The Greenland Ice Sheet Project 2 depth-age scale: methods and results. J. Geophys. Res. 102, 26411–26423. http://dx.doi.org/10.1029/97JC00269.

Morales, J.A., Borrego, J., San Miguel, E.G., López-González, N., Carro, B., 2008. Sedimentary record of recent tsunamis in the Huelva Estuary (southwestern Spain). Quat. Sci. Rev. 27, 734–746. http://dx.doi.org/10.1016/j.quascirev.2007.12.002.

Nelson, C.H., Baraza, J., Maldonado, A., 1993. Mediterranean undercurrent sandy contourites, Gulf of Cadiz, Spain. Sediment. Geol. 82, 103–131. http://dx.doi.org/10.1016/0037-0738(93)90116-M.

Nelson, C.H., Baraza, J., Maldonado, A., Rodero, J., Escutia, C., Barber Jr., J.H., 1999. Influence of the Atlantic inflow and Mediterranean outflow currents on late Quaternary sedimentary facies of Gulf of Cádiz continental margin. Mar. Geol. 155, 99–129. http://dx.doi.org/10.1016/S0025-3227(98)00143-1.

Niitani, S., Masuda, F., Naruse, H., 2013. Tsunami-induced gravity currents generated in an experimental flume. J. Sedimentol. Soc. Jpn. 72, 109–113. http://dx.doi.org/10.4096/jssj.72.109 (in Japanese with English abstract).

Rebesco, M., Camerlenghi, A., Van Loon, A.J., 2008. Contourite. Development in Sedimentology 60. Elsevier, Amsterdam (663 pp.).

Rebesco, M., Hernández-Molina, F.J., Van Rooij, D., Wåhlin, A., 2014. Contourites and associated sediments controlled by deep-water circulation processes: state of the art and future considerations. Mar. Geol. 352, 111–154. http://dx.doi.org/10.1016/j.margeo.2014.03.011.

Reimer, P., Bard, E., Bayliss, A., Beck, J., Blackwell, P., Bronk Ramsey, C., Buck, C., Cheng, H., Edwards, R., Friedrich, M., Grootes, P., Guilderson, T., Haflidason, H., Hajdas, I., Hatté, C., Heaton, T., Hoffmann, D., Hogg, A., Hughen, K., Kaiser, K., Kromer, B., Manning, S., Niu, M., Reimer, R., Richards, D., Scott, E., Southon, J., Staff, R., Turney, C., van der Plicht, J., 2013. IntCal13 and Marine13 radiocarbon age calibration curves 0–50,000 years cal BP. Radiocarbon 55, 1869–1887. http://dx.doi.org/10.2458/azu_js_rc.55.16947.

Rodríguez-Tovar, F.J., Dorador, J., 2014. Ichnological analysis of Pleistocene sediments from the IODP Site U1385 "Shackleton Site" on the Iberian Margin: approaching palaeoenvironmental conditions. Palaeogeogr. Palaeoclimatol. Palaeoecol. 409, 24–32. http://dx.doi.org/10.1016/j.palaeo.2014.04.027.

Rodríguez-Tovar, F.J., Dorador, J., 2015. Ichnofabric characterization in cores: a method of digital image treatment. Ann. Soc. Geol. Pol. (in press).

Rodríguez-Vidal, J., Ruiz, F., Cáceres, L.M., Abad, M., González-Regalado, M.L., Pozo, M., Carretero, M.I., Monge, A.M., Gómez, F., 2011. Geomarkers of the 218–209 BC Atlantic tsunami in the Roman Lacus Ligustinus (SW Spain): a palaeogeographical approach. Quat. Int. 242, 201–212. http://dx.doi.org/10.1016/j.quaint.2011.01.032.

Rogerson, M., Rohling, E.J., Bigg, G.R., Ramirez, J., 2012. Paleoceanography of the Atlantic–Mediterranean exchange: overview and first quantitative assessment of climatic forcing. Rev. Geophys. 50, RG2003. http://dx.doi.org/10.1029/2011RG000376.

Shanmugam, G., 2006a. Deep-Water Processes and Facies Models: Implications for Sandstone Petroleum Reservoirs. Handbook of Petroleum Exploration and Production 5. Elsevier, Amsterdam (496 pp.).

Shanmugam, G., 2006b. The tsunamite problem. J. Sediment. Res. 76, 718–730. http://dx.doi.org/10.2110/jsr.2006.073.

Shanmugam, G., 2008. Deep-Water Bottom Currents and Their Deposits. In: Rebesco, E., Camerlenghi, A. (Eds.), Contourites. Elsevier, Amsterdam, pp. 59–81.

Shanmugam, G., 2012. New Perspectives on Deep-Water Sandstones: Origin, Recognition, Initiation and Reservoir Quality. Handbook of Petroleum Exploration and Production 9. Elsevier, Amsterdam (488 pp.).

Shanmugam, G., Spalding, T.D., Rofheart, D.H., 1993. Traction structures in deep-marine bottom-current reworked sands in the Pliocene and Pleistocene, Gulf of Mexico. Geology 21, 929–932. http://dx.doi.org/10.1130/0091-7613(1993)021<0929:TSIDMB>2.3.CO;2.

Sirviö, T., Kajander, M., 2003. Holocene development of the Pennala basin with special reference to the palaeoenvironment of Meso- and Neolithic dwelling sites, Lahti–Orimattila, Southern Finland. Fennia 181, 85–101.

Smith, D.E., Shi, S., Cullingford, R.A., Dawson, A.G., Dawson, S., Firth, C.R., Foster, I.D.L., Fretwell, P.T., Haggart, B.A., Holloway, L.K., Long, D., 2004. The Holocene Storegga Slide tsunami in the United Kingdom. Quat. Sci. Rev. 23, 2291–2321. http://dx.doi.org/10.1016/j.quascirev.2004.04.001.

Stich, D., Ammon, C.J., Morales, J., 2003. Moment tensor solutions for small and moderate earthquakes in the Ibero-Maghreb region. J. Geophys. Res. 108, 2148–2168. http://dx.doi.org/10.1029/2002JB002057.

Stich, D., Mancilla, F., Morales, J., 2005. Crust–mantle coupling in the Gulf of Cadiz (SW Iberia). Geophys. Res. Lett. 32, L13306. http://dx.doi.org/10.1029/2005GL023098.

Stow, D.A.V., Faugères, J.-C., 2008. Contourite Facies and the Facies Model. In: Rebesco, E., Camerlenghi, A. (Eds.), Contourites. Elsevier, Amsterdam, pp. 143–156.

Stow, D.A.V., Faugères, J.-C., Gonthier, E., 1986. Facies distribution and textural variation in Faro Drift contourites: velocity fluctuation and drift growth. Mar. Geol. 72, 71–100. http://dx.doi.org/10.1016/0025-3227(86)90100-3.

Stow, D.A.V., Faugères, J.-C., Gonthier, E., Cremer, M., Llave, E., Hernández-Molina, F.J., Somoza, L., Díaz del Río, V., 2002. Faro-Albufeira drift complex, northern Gulf of Cádiz. Mem. Geol. Soc. Lond. 22, 137–154. http://dx.doi.org/10.1144/GSL.MEM.2002.022.01.11.

Stow, D.A.V., Hernández-Molina, F.J., Alvarez Zarikian, C.A., the Expedition 339 Scientists, 2013b. Proceedings IODP 339. Integrated Ocean Drilling Program Management International, Tokyo. http://dx.doi.org/10.2204/iodp.proc.339.2013.

Stow, D.A.V., Hernández-Molina, F.J., Llave, E., Bruno, M., García, M., Díaz del Río, V., Somoza, L., Brackenridge, R.E., 2013a. The Cadiz Contourite Channel: sandy contourites, bedforms and dynamic current interaction. Mar. Geol. 343, 99–114.

Stow, D.A.V., Lovell, J.P.B., 1979. Contourites: their recognition in modern and ancient sediments. Earth-Sci. Rev. 14, 251–291. http://dx.doi.org/10.1016/0012-8252(79)90002-3.

Stow, D.A.V., Piper, D.J.W., 1984. Deep-Water Fine-Grained Sediments: Facies Models. In: Stow, D.A.V., Piper, D.J.W. (Eds.), Fine-Grained Sediments: Deep-Water Processes and Facies. Geological Society of London Special Publication 15, pp. 611–646.

Stow, D.A.V., Wilkinson, H.D., Hernández-Molina, F.J., 2008. The Nature of Contourite Deposition. In: Rebesco, E., Camerlenghi, A. (Eds.), Contourites. Elsevier, Amsterdam, pp. 223–250.

Stuiver, M., Reimer, P.J., 1993. Extended ^{14}C database and revised CALIB radiocarbon calibration program. Radiocarbon 35, 215–230.

Sugawara, D., Goto, K., 2012. Numerical modeling of the 2011 Tohoku-oki tsunami in the offshore and onshore of Sendai Plain, Japan. Sediment. Geol. 282, 110–123. http://dx.doi.org/10.1016/j.sedgeo.2012.08.002.

Talma, A., Vogel, J., 1993. A simplified approach to calibrating ^{14}C dates. Radiocarbon 35, 317–322.

Toucanne, S., Mulder, T., Schönfeld, J., Hanquiez, V., Gonthier, E., Duprat, J., Cremer, M., Zaragosi, S., 2007. Contourites of the Gulf of Cadiz: a high-resolution record of the paleocirculation of the Mediterranean outflow water during the last 50,000 years. Palaeogeogr. Palaeoclimatol. Palaeoecol. 246, 354–366. http://dx.doi.org/10.1016/j.palaeo.2006.10.007.

Udías, A., López Arroyo, A., Mezcua, J., 1976. Seismotectonic of the Azores–Alboran Region. Tectonophysics 31, 259–289. http://dx.doi.org/10.1016/0040-1951(76)90121-9.

Viana-Baptista, M.A., Soares, P.M., Miranda, J.M., Luis, J.F., 2006. Tsunami propagation along Tagus estuary (Lisbon, Portugal) preliminary results. Sci. Tsunami Haz. 24, 329–338.

Voelker, A.H.L., Lebreiro, S.M., Schonfeld, J., Cacho, I., Erlenkeuser, H., Abrantes, F., 2006. Mediterranean outflow strengthening during northern hemisphere coolings: a salt source for the glacial Atlantic? Earth Planet. Sci. Lett. 245, 39–55. http://dx.doi.org/10.1016/j.epsl.2006.03.014.

Whelan, F., Kelletat, D., 2005. Boulder deposits on the southern Spanish Atlantic coast: possible evidence for the 1755 AD Lisbon tsunami? Sci. Tsunami Haz. 23, 25–38.

Wright, S.G., Rathje, E.M., 2003. Triggering mechanisms of slope instability and their relationship to earthquakes and tsunamis. Pure Appl. Geophys. 160, 1865–1877. http://dx.doi.org/10.1007/s00024-003-2410-4.

Zitellini, N., Gràcia, E., Matias, L., Terrinha, P., Abreu, M.A., DeAlteriis, G., Henriet, J.P., Dañobeitia, J.J., Masson, D.G., Mulder, T., Ramella, R., Somoza, L., Diez, S., 2009. The quest for the Africa–Eurasia plate boundary west of the Strait of Gibraltar. Earth Planet. Sci. Lett. 280, 13–50. http://dx.doi.org/10.1016/j.epsl.2008.12.005.